Dynamic stress analysis of rock joints under railway loading

Marlisio Oliveira Cecilio Junior, MSc
School of Civil and Environmental Engineering, Faculty of Engineering and Information Technology, University of Technology Sydney, Sydney, Australia
email: marlisio.cecilio@student.uts.edu.au
ORCID number: 0009-0001-7794-1461

Buddhima Indraratna, PhD, FTSE, FIEAust., FASCE, FGS, CPEng
School of Civil and Environmental Engineering, Faculty of Engineering and Information Technology, University of Technology Sydney, Sydney, Australia
email: buddhima.indraratna@uts.edu.au
ORCID number: 0000-0002-9057-1514

Cholachat Rujikiatkamjorn, PhD, CPEng, FIEAust, MASCE
School of Civil and Environmental Engineering, Faculty of Engineering and Information Technology, University of Technology Sydney, Sydney, Australia
email: cholachat.rujikiatkamjorn@uts.edu.au
ORCID number: 0000-0001-8625-2839

Rakesh Sai Malisetty, PhD
School of Civil and Environmental Engineering, Faculty of Engineering and Information Technology, University of Technology Sydney, Sydney, Australia
email: rakeshsai.malisetty@uts.edu.au
ORCID number: 0000-0001-8872-2670

Full contact details of corresponding author
Buddhima Indraratna
School of Civil and Environmental Engineering - UTS
81-113 Broadway, Ultimo, NSW - Australia, zip code 2007
Phone: +61 2 9514 8000; Mobile: +61 400 213 046
email: buddhima.indraratna@uts.edu.au

Date the text was last revised: **30/Jan/2024**
Number of words in the main text: **6,669**
Number of figures: **15**
Number of tables: **2**

Abstract

The proper estimation of stresses generated by train passage is of fundamental importance for the serviceability and longevity of railways, and yet very limited knowledge is available where the track substructure is built on a jointed rock mass. The present study introduces an analytical solution for estimating the ground stresses arising from moving wheel loads, causing a change in the three-dimensional stress state in the track formation, in relation to the stress variation with depth and along the longitudinal track section, i.e. the direction of train passage. Based on 21 case histories, an array of field measurements and numerical simulations covering a wide range of freight tonnage, train speeds, and different formation conditions, were considered to validate the proposed analytical solution. The proposed methodology (analytical solution) was then applied to a jointed rock subgrade to determine the normal and shear stresses acting along a specific discontinuity plane. The main analytical outcome demonstrates that the orthogonal vertical and shear stresses present different and phase-shifted history plots for homogeneous ground conditions with principal stresses rotation. However, conversely for a jointed subgrade, the normal and shear stresses along the discontinuity have the same history plot pattern and are in phase. As a practical guide, the results from this study would help to define which cyclic loads should be applied in laboratory tests to simulate realistic traffic patterns of trains travelling over a jointed rock subgrade.

Keywords

Design methods, Joints, Railway tracks, Rock, Stress analysis

List of notations

B	width of the sleeper
$CNSR$	cyclic normal stress ratio
d_1	longitudinal distance between consecutive axles from the same bogie
d_2	longitudinal distance between axles from adjacent bogies
d_3	longitudinal distance between axles from same-wagon bogies
D	wheel diameter of the train
DAF	dynamic amplification factor
E	Young's modulus of the steel rail
E_i	elasticity modulus of the ith layer of the track's substructure
f	frequency of the cyclic stress pulse
F_i	concentrated force on top of the sleeper "i"
h_{eq}	equivalent thickness of the multi-layer structure
h_i	thickness of the ith layer of the track's substructure
i, j, k	orthogonal unit vectors respectively along the X, Y and Z directions
I	moment of inertia of the steel rail
I_f	influence factor that multiplies the pressure applied by the sleeper
$I_f^{(-)}$	influence factor for the areas outside the footprint of the loaded area
$I_f^{(+)}$	influence factor for the loaded areas
k	linear proportionality constant of the springs, the track modulus
K	horizontal to vertical stress ratio prior to the cyclic load
K_0	earth pressure coefficient at rest
L	sleeper's length
n	sleeper's number
N	number of the lowest layer of the track's substructure (subgrade)
$p(x)$	distributed reaction underneath the rail
p_0	mean (octahedral) stress prior to the cyclic load
P_i	vertical pressure underneath the sleeper "i"
S	longitudinal spacing between sleepers
t	time

V	train speed
W	concentrated force of one wheel
W_{dyn}	dynamic wheel load
W_{sta}	static wheel load
x, y, z	longitudinal, transverse and vertical distances, respectively
X, Y, Z	longitudinal (train passage), transverse and vertical directions/axes, respectively
x_i	longitudinal distance from the sleeper "i" centreline to the wheel load
$x_i^{(-)}$	lower integration limit of p(x)
$x_i^{(+)}$	upper integration limit of p(x)
α	angle of principal stresses rotation
β	coefficient for the rail vertical displacement profile
δ	rail vertical displacement
$\Delta\sigma_a$	incremental cyclic axial stress in triaxial tests
$\Delta\sigma_x$	incremental orthogonal longitudinal stress
$\Delta\sigma_y$	incremental orthogonal transverse stress
$\Delta\sigma_z$	incremental orthogonal vertical stress
$\Delta\tau_{xy}$	incremental shear stress on the horizontal plane
$\Delta\tau_{xz}$	incremental shear stress on the vertical/longitudinal plane
$\Delta\tau_{yz}$	incremental shear stress on the vertical/transverse plane
η	ratio between the maximum increments of shear and normal stresses
$\eta_{triaxial}$	shear-to-normal stress ratio in triaxial tests
θ_D	dip angle of the discontinuity plane
θ_S	strike angle of the discontinuity plane
ν_i	Poisson's ratio of the ith layer of the track's substructure
σ_{calc}	stress calculated using the proposed analytical solution
σ_n	normal stress on the discontinuity plane
σ_{ref}	stress disclosed by the reference of each case study
τ	shear stress on the discontinuity plane
φ_b	basic friction angle of the joint

1. Introduction

A jointed rock mass includes discontinuities such as fault planes, joints, bedding planes and other planes of weakness. In such a case, the properties of discontinuities usually govern the subgrade behaviour, which is comprised of a matrix of discreet blocks interacting with each other. Therefore, the reliability of civil works built near or within a jointed rock formation depends on how well one understands the behaviour of the said discontinuities.

Various experimental and numerical studies have been conducted in the past to comprehend the behaviour of rock joints mostly under static loads, such as for rock slopes, open pit mining, tunnelling and underground excavations (Indraratna *et al.*, 2010a; Thirukumaran *et al.*, 2016; Casagrande *et al.*, 2018; Jeffery *et al.*, 2022), but these are not appropriate for realistic train traffic loading which tends to be cyclic. Only limited research, however, has been carried out considering proper dynamic loads. For instance, direct shear tests on rock joints were carried out by Barbero *et al.* (1996) and Wang *et al.* (2016) applying dynamic, monotonic loading, while Hsiung *et al.* (1993, 1994) and Fathi *et al.* (2016) applied dynamic, cyclic loads. Dang *et al.* (2016, 2018) carried out direct shear tests where the cyclic loads were applied in the normal (vertical) direction. However, in these studies, the applied loads were still different to typical railway conditions characterised by moving axle loads. In addition, triaxial tests on jointed rock samples subjected to cyclic axial loads were performed by Jafari *et al.* (2003), Liu & Liu (2017), Liu & Dai (2018), Indraratna *et al.* (2021), Soomro *et al.* (2022) and Peellage *et al.* (2022). In general, most geotechnical laboratory studies (e.g. shear box and triaxial testing) have obvious limitations as their test boundary conditions cannot accurately mimic the type of moving train loading with principal axes rotation, hence the need for greater focus on mathematical (analytical) modelling to supplement such experimental outcomes. Moreover, the majority of the aforementioned dynamic loads had meant to represent vibrations and deformations caused by earthquakes and rock blasting, while only some limited studies, for instance by Indraratna *et al.* (2021), Soomro *et al.* (2022) and Peellage *et al.* (2022) have been more closely related to typical railway (cyclic) loading.

When a railway is constructed over a jointed rock formation that is not properly stabilised, there will be an accumulation of permanent, plastic shear displacements along the discontinuity plane over time. This may result in the occurrence of differential settlements and track misalignment, displacement of sleepers, damage to rail-sleeper fasteners, and even rail buckling, leading to substantial maintenance, repair works, and traffic interruptions associated with a notable loss of productivity.

One crucial step for railway design, therefore, is to estimate the additional ground stresses caused by the traffic load. Although the analytical prediction of stresses in an elastic, homogeneous subgrade is not a new topic, past contributions present serious limitations in relation to the adopted hypotheses and the simplifications made in emulating the actual loading patterns. For instance, the vast majority of analytical solutions solely address the vertical stress increment (Bathurst & Kerr, 1999; Esveld, 2001). While the vertical stress component is certainly predominant, the variation of other stress components (e.g. shear stress along the vertical/longitudinal plane) may result in a significant change of stress paths as well as the rotation of principal stresses, influencing the mechanical response of the subgrade during the passage of a train (Brown, 1996; Momoya *et al.*, 2005; Powrie *et al.*, 2007; Indraratna *et al.*, 2011; Powrie *et al.*, 2019). Some solutions estimate the vertical stress along the vertical projection of the train wheel by assuming a certain percentage of the train load (Jeffs & Tew, 1991; Wang *et al.*, 2020), instead of accounting for the actual load distribution under the rail along its longitudinal direction. Moreover, the majority of existing analytical solutions consider the ground as a homogeneous, infinite elastic half-space, whereas only a few solutions attempt to incorporate the characteristics of a layered track substructure (Odemark, 1949; Kandaurov, 1966).

Recognising the aforementioned limitations and inaccuracies, in this paper the authors have made an attempt to present a simple and practical analytical solution that does not require any cumbersome, numerical iterations. This paper demonstrates how this novel analytical solution can be successfully applied to a railway built over a jointed rock foundation, capturing the moving load effect on the response of the discontinuities. To the authors' knowledge, there is currently no comprehensive analytical solution for the determination of stresses along rock discontinuities subjected to moving train loads.

2. Proposed analytical approach

The present approach focuses on determining the three-dimensional stress state caused by the moving load beneath a rail track. In this study, the adopted procedures incorporate the integration of different fundamental contributions from Bathurst & Kerr (1999), Indraratna *et al.* (2011) and AREMA (2019), and can be divided into distinct steps at three different substructure interfaces:

i) calculating the vertical distributed load at the base of the rail, due to the train load,
ii) determining the vertical pressure underneath the sleepers, due to the rail load, and
iii) calculating the incremental three-dimensional stresses in the substructure including the subgrade.

2.1 Distributed load under the rail

The first step considers an infinitely long elastic beam subjected to a concentrated force, supported by Winkler springs, resulting in a "continuous" distributed reaction along the rail bottom. The elastic beam solution assumes that: (a) the effect of eventual axial forces acting in the rail is negligible, and (b) the rail is not subjected to horizontal moments or torque caused by its interaction between the fasteners and/or sleepers. Bathurst & Kerr (1999) have justified both these assumptions to determine the stresses generated in the ballast and subgrade. Schwedler (1882) solved the differential equation for the vertical displacement **δ** of such an elastic beam, i.e. the well-known classical equation given by:

$$EI\frac{d^4\delta(x)}{dx^4} + k.\delta(x) = W(x) \tag{1}$$

where $\boldsymbol{x}$ is the rail axial axis (track longitudinal direction), $\boldsymbol{W(x)}$ is the distribution of vertical wheel loads on the rail, $\boldsymbol{EI}$ is the rail flexural stiffness in the vertical/longitudinal plane, and $\boldsymbol{k}$ is the linear proportionality constant of the springs (with units of force / rail deflection / rail length), also referred to as the ground reaction or "track modulus". The support provided by the springs represents the collective response of the rail fasteners, sleepers, ballast, subgrade and other substructures. The vertical displacement profile of the rail is represented as a function of the coefficient $\boldsymbol{\beta}$ (length^{-1}), hence,

$$\delta(x) = \frac{W\beta}{2k} e^{-\beta|x|} [\cos(\beta|x|) + \sin(\beta|x|)] \tag{2}$$

$$\beta = \sqrt[4]{\frac{k}{4EI}} \tag{3}$$

for the concentrated force of one wheel (***W***) and the boundary conditions δ(∞) = 0, δ'(0) = 0, and δ"(0) = P/(2EI). The distributed reaction underneath the rail, ***p(x)***, can then be expressed as:

$$p(x) = \frac{W\beta}{2} e^{-\beta|x|} [\cos(\beta|x|) + \sin(\beta|x|)] \tag{4}$$

The present study considers values of track modulus obtained after field measurements. In their absence, the spring constant (***k***) is determined through a back-analysis using Eq. 2 having a known longitudinal profile of measured rail vertical displacement, ***δ(x)***. As an alternative, ***k*** may be adopted according to available data from other locations with similar conditions, for instance, the values presented by Esveld (2001). A distinction must be made for the single wheel load considered in Eq. 4, which could be either a static or a dynamic load. The former ($\boldsymbol{W_{sta}}$) is related to the train tonnage and its number of axles, while the latter ($\boldsymbol{W_{dyn}}$) also considers the train speed by multiplying the static load by a dynamic amplification factor (DAF). Previous studies have compared field measurements of dynamic wheel loads to known static ones, expressing the values of DAF as a function of the train speed (e.g. Li & Selig, 1998; Esveld, 2001; Sun *et al.*, 2016). In contrast, the present study has adopted the expressions proposed by Nimbalkar & Indraratna (2016), also taking into account the type of subgrade:

$$DAF = 1 + 0.0052(V/D)^{0.755} \quad \text{for soil subgrade} \tag{5}$$

$$DAF = 1 + 0.0065(V/D)^{1.005} \quad \text{for rock subgrade} \tag{6}$$

where the train speed ***V*** is expressed in km/h and the wheel diameter ***D*** in meters.

2.2 Stress under the sleepers

The present solution considers a concentrated force $\boldsymbol{F_i}$ on top of each sleeper, which is determined by integrating the distributed load ***p(x)*** from Eq. 4, within the limits $\boldsymbol{x_i^{(-)}}$ and $\boldsymbol{x_i^{(+)}}$:

$$F_i = \int_{x_i^{(-)}}^{x_i^{(+)}} p(x) = \frac{W\,\beta}{2}\left[\left(e^{-\beta\, x_i^{(+)}}\,\frac{-\cos\left(\beta\, x_i^{(+)}\right)}{\beta}\right) - \left(e^{-\beta\, x_i^{(-)}}\,\frac{-\cos\left(\beta\, x_i^{(-)}\right)}{\beta}\right)\right] \tag{7}$$

$$x_i^{(-)} = x_i - (S/2) \quad \text{and} \quad x_i^{(+)} = x_i + (S/2) \tag{8}$$

where $\boldsymbol{x_i}$ is the distance from the sleeper "i" centreline to the wheel load ***W*** along the track longitudinal direction, and ***S*** is the sleepers' spacing. It is observed that in case the area under the distributed load curve is approximated by a rectangle with a base equal to the sleeper spacing, then the calculated forces on top of the sleepers are overestimated.

The concentrated force $\boldsymbol{F_i}$ from Eq. 7 is then transferred to the base of the sleeper to determine the stress applied on top of the ballast layer. According to Shenton (1975) and Bathurst & Kerr (1999), the distribution of the vertical pressure underneath the sleeper varies considerably even with slight changes in track properties, including the substructure layers of subgrade, ballast, sleepers and fasteners, as well as the stress changes attributed to uneven freight distributions of the moving trains. Some studies have either simulated the stress distribution numerically (Priest *et al.*, 2010; Xu *et al.*, 2018) or measured in the field the vertical stress profile below the sleeper along its axial direction (Shenton, 1975; Nie *et al.*, 2005). Most studies have established that the vertical stress is usually higher under the direct projection of the rails, then reduced at the edges of the sleeper, and considerably smaller (often negligible) towards the middle of the sleeper. This solution considers the vertical pressure underneath each sleeper $\boldsymbol{P_i}$ as uniformly distributed on a rectangular area equivalent to the outer thirds of the sleeper base:

$$P_i = F_i / [B.(L/3)] \quad (9)$$

where $\boldsymbol{B}$ is the sleeper's width and $\boldsymbol{L}$ is its length.

Considering the area as uniformly loaded, one often ignores the flexural stiffness of the sleepers, which is another reason for the aforementioned variation in the vertical pressure. According to Indraratna *et al.* (2011) and Wang *et al.* (2020), the prediction of stresses using analytical solutions under such an assumption is commonly overestimated when compared to field measurements.

2.3 Three-dimensional stresses in the substructure layers and subgrade

Boussinesq (1883) determined the incremental three-dimensional stress state acting at any point below the surface caused by a superficial point load. Newmark (1935) integrated Boussinesq's solution across a uniformly loaded rectangular area, which in this study represents the pressure exerted by the sleeper. The incremental vertical stress $\boldsymbol{\Delta\sigma_z}$ thus obtained for points of interest along the vertical projection of a rectangle corner is calculated using Eqs. A1 and A2 from the Appendix. Holl (1940) then integrated Boussinesq's solution for the same boundary conditions, obtaining the incremental stresses for the remaining directions using Eqs. A3 to A8 from the Appendix: horizontal longitudinal and transverse stresses, $\boldsymbol{\Delta\sigma_x}$ and $\boldsymbol{\Delta\sigma_y}$, and shear stresses on the vertical/longitudinal, vertical/transverse and horizontal planes, respectively $\boldsymbol{\Delta\tau_{xz}}$, $\boldsymbol{\Delta\tau_{yz}}$, and $\boldsymbol{\Delta\tau_{xy}}$.

Bearing in mind that this solution is linear, the contribution of adjacent sleepers is accounted for by considering the principle of superposition, as detailed in the Appendix. Boussinesq's analytical solution assumes a homogenous, isotropic, linearly elastic, infinite half-space as the medium where the stresses are calculated. The mechanical behaviour of the ballast and subgrade could be fairly represented as linearly elastic, however, railways have a layered structure acting as a heterogeneous, anisotropic, finite medium. To overcome such a limitation, the present study converts the multi-layered structure into an equivalent single-layer medium. Odemark (1949) proposed the following equation to determine the equivalent thickness $\boldsymbol{h_{eq}}$ of the single layer, based on the properties of each layer and having the lowest one, number $\boldsymbol{N}$, as the subgrade:

$$h_{eq}=\left[h_1\left(\frac{E_1}{E_N}\cdot\frac{1-v_N^2}{1-v_1^2}\right)^{1/3}+h_2\left(\frac{E_2}{E_N}\cdot\frac{1-v_N^2}{1-v_2^2}\right)^{1/3}+\ldots+h_{N-1}\left(\frac{E_{N-1}}{E_N}\cdot\frac{1-v_N^2}{1-v_{N-1}^2}\right)^{1/3}\right] \quad (10)$$

where $\boldsymbol{h_i}$, $\boldsymbol{E_i}$ and $\boldsymbol{v_i}$ are respectively the thickness, the elasticity modulus and the Poisson's ratio of the ith layer. According to Indraratna *et al.* (2011), this approximation is valid only for cases where the elastic moduli decrease with depth, as well as the equivalent thickness of each layer is larger than the equivalent radius of the loaded area. Another multi-layer equivalency by Kandaurov (1966) considers only the earth pressure coefficient at rest ($\boldsymbol{K_0}$) and with no restrictions regarding layer thickness, soil properties or the stress state of any substructure layer:

$$h_{eq}=h_1\left(\frac{K_{0_1}}{K_{0N}}\right)^{1/2}+h_2\left(\frac{K_{0_2}}{K_{0N}}\right)^{1/2}+\ldots+h_{N-1}\left(\frac{K_{0N-1}}{K_{0N}}\right)^{1/2} \quad (11)$$

A flowchart is provided in Figure 1 as a summary of the calculation steps and input parameters required by the proposed analytical solution.

3. Validation of the analytical solution

The proposed analytical solution is validated using data from field measurements (F), laboratory physical models (L), and numerical analyses (N), as tabulated in Table 1, where each case study is numbered for ease of reference. Cases 1 to 17 provide measurements of vertical stresses from both field and lab monitoring, while Cases 18 to 21 provide stresses calculated after 2D and 3D numerical (FEM) models. It is noteworthy that the latter were validated using measured track and ground displacements, and that other publications were not included herein as they did not adopt such an approach.

The track substructure of each case study is presented in Table 1, including the thickness and properties of each layer. The analyses of railways built over a subgrade stiffer than the ballast (Cases 3, 5, 9, 10, 14, 16, 17, and 18) considered Kandaurov's multi-layer equivalency (Eq. 11) and the disclosed values of earth pressure coefficient at rest (***K₀***). For the remaining cases, with the stiffness of layers decreasing with depth, the analyses did consider Odemark's equation (Eq. 10) and the disclosed values of elasticity modulus (***E***) and Poisson's ratio (***v***). Table 1 also presents the values of ground reaction (***k***) considered for each analysis, varying from 10 to 200 MN/m^2, noticeably higher for rock subgrade and lower for softer soil.

Table 2 presents the analyses carried out for each case study, where one may observe a relatively wide range of train tonnages and velocities varying from 10.5 to 35 t/axle and 0 to 360 km/h, respectively. The rail properties and the sleeper dimensions considered for each analysis are also disclosed in Table 2. The stresses were calculated at depths varying from 0 to 3.45 m measured from the base of the sleeper, with varying track substructure conditions and different types of subgrades. Table 2 also presents the calculated stresses using the proposed analytical solution for all case studies (σ_{calc}) and the values disclosed by their respective publications, namely the reference stresses (σ_{ref}).

The calculated stresses (σ_{calc}) from Cases 2 and 3 demonstrate how the proposed analytical solution can capture the influence of different subgrade conditions. Although both cases considered the same train tonnage and speed, rail properties and sleeper dimensions, the one with a stiffer subgrade (higher ground reaction coefficient, ***k***) resulted in higher vertical stresses. Such influence is corroborated by the field measurements (σ_{ref}) by Indraratna *et al.* (2014) and Nimbalkar & Indraratna (2016).

Figure 2 (a) presents a comparison between σ_{calc} and σ_{ref} where an overall agreement is observed, thus validating the analytical solution. The linear regression of all 99 pairs of σ_{calc} and σ_{ref} resulted in a coefficient of determination R^2 = 0.996 for σ_{calc} = 1.007 σ_{ref}. To further improve the present validation, values of calculated per reference stress ($\sigma_{calc}/\sigma_{ref}$) were scrutinised, as the closer the ratio is to unity, the more accurate the analytical solution. A statistical analysis is presented in Figure 2 (b), with the cumulative probability of occurrence of $\sigma_{calc}/\sigma_{ref}$. The mean value and standard deviation are respectively 1.04 and 0.09, which demonstrates that the analytical solution slightly overestimates the stresses by 4% on average. With 68.8% of $\sigma_{calc}/\sigma_{ref}$

equal to or higher than unity, the analytical solution may be considered conservative. A ratio of 1.01 was obtained as the mode value, which is the most frequent occurrence. The data are within the lower and upper bounds of 0.89 and 1.21, respectively for 5% and 95% reliability. Figure 2 (b) also presents a log-normal probability distribution adjusted to these results, adopted after the statistical Kolmogorov-Smirnov adherence test (Massey, 1951). Figure 2 (c) demonstrates how the values of $\boldsymbol{\sigma_{calc}/\sigma_{ref}}$ vary with depth. It is clear how the analytical prediction is more accurate immediately beneath the sleepers (z = 0 m) and how its variability is greater with depth. This is due to the increase in the number of variables and assumptions required for the third step of the analytical solution (e.g., parameters for Boussinesq's equations and the multi-layer equivalent medium). Nonetheless, it was not possible to find a proper trend for how the variability of $\boldsymbol{\sigma_{calc}/\sigma_{ref}}$ is influenced by depth, which is confirmed by the statistical tests of covariance and correlation coefficient, as they both resulted near zero.

The solution's tendency to slightly overestimate the results may be explained by some of its assumptions (e.g. disregarding the sleepers' flexural rigidity), but also the reliability of *in-situ* measurements. Priest et al. (2010) argued that the validity of *in-situ* measurements would depend on the relative stiffness between the pressure cell and the surrounding medium, besides the adopted installation procedures, and Shenton (1975) that the accuracy of stress measurement in the ballast layer is directly influenced by the reduced number of contact points within the ballast.

4. Application of the analytical solution

A hypothetical railway constructed over a jointed rock mass subgrade is considered here to demonstrate the application of the proposed analytical solution to a practical situation on the eastern coast of Australia. The standard gauge track is comprised of 60kg/m steel rails (Australian standards) with Young's modulus of E = 210 GPa and moment of inertia of I = 29.50×10^{-6} m^4, concrete sleepers (2.50 m long and 0.26 m wide) spaced every 0.60 m, over a 0.30 m thick ballast layer. The subgrade below the ballast layer is the Hawkesbury sandstone, which is a near-surface geological formation in the Sydney metropolitan area and along the freight rail route along the Eastern coast in the state of New South Wales. For simplicity, the discontinuities present in the Hawkesbury sandstone are considered as relatively clean joints with negligible cohesion (no infilled sediments) and with a basic friction angle $\varphi_b = 40°$ (Pells, 2004; Bertuzzi, 2016). The collective response of sleepers, ballast, and subgrade is represented by the ground reaction coefficient k = 150 MN/m^2, which was adopted based on values from the case studies with rock subgrade in the validation chapter. Three different types of trains traversing these tracks are considered:

- Case A) heavy-haul of coal, 25 tonnes at 80 km/h,
- Case B) express freight, 20 tonnes at 115 km/h, and
- Case C) passenger trains, 15 tonnes at 200 km/h (still in discussion by Sydney Trains).

All the above trains have a wheel composition of 2 bogies and 4 axles per wagon, longitudinal distances between axles $d_1 = 1.72$ m (same bogie), $d_2 = 2.10$ m (adjacent bogies), and $d_3 = 8.40$ m (same-wagon bogies). The maximum velocities for the freight trains were limited by the recommendation of the Australian Rail Track Corporation Limited (ARTC, 2022).

4.1 Homogeneous rock subgrade

The three-dimensional stresses acting on the ballast and subgrade are calculated initially considering an intact sandstone with no prominent discontinuities. The vertical and shear stress histories, $\Delta\sigma_z$ and $\Delta\tau_{xz}$, due to a single wheel load, rendered a vertical stress peak corresponding to a null shear stress at the alignment of the load at the point of calculations, whereas the peak of shear stress is anticipated by $\pi/2$ and changes its sign after the passage of the load. Such a pattern is consistent with published outcomes (e.g. Brown, 1996; Momoya *et al.*, 2005; Powrie *et al.*, 2007; Powrie *et al.*, 2019; *Qian et al., 2016;* Guo *et al.*, 2018).

The variation of stress with time is significantly altered when multiple axles are considered, as presented in Figure 3, corroborating the importance of capturing the longitudinal distance between the axles. These stress histories were calculated for Case A (25t at 80km/h) at three different depths measured from the base of the sleeper: (a) 0.3 m, i.e. at the ballast/subgrade interface, (b) 0.6 m, and (c) 1.0 m. For the shallow depth analysis considered in (a), the stress pulses directly correspond to the passage of each axle with a well-marked "M" shape, whereas for the deeper analysis in the case of (c), the responses from four axles of two adjacent bogies may be approximated well by a single stress pulse. For the above conditions, the cyclic stresses may be represented with a frequency of f=12.9 Hz at z=0.3m (related to the distance between consecutive axles), 5.8 Hz at z=0.6m (distance of adjacent bogies), or 1.6 Hz at z=1.0m (wagon length). Similarly, for the same depths, Case B (20t at 115km/h) may be simulated with f=18.6, 8.4, and 2.3 Hz cyclic stress pulses, and Case C (15t at 200km/h) with f=32.3, 14.5, and 4.0 Hz. Such attenuation of the frequency with depth is corroborated by either past field measurements (Gräbe *et al.*, 2005; Liu & Xiao, 2010; Zhang *et al.*, 2016) or numerical simulations (Powrie *et al.*, 2007; Priest *et al.*, 2010; Xu *et al.*, 2018; Zhao *et al.*, 2021; Tucho *et al.*, 2022). Figure 3 also includes an insert illustrating the distances d_1, d_2, and d_3, which were previously defined upon the presentation of Cases A, B and C trains.

Figure 4 presents how the maximum value of incremental stresses varies with depth, for the three cases of train loads. As observed from the plotted data, the horizontal stresses $\Delta\sigma_x$ and $\Delta\sigma_y$ are substantially reduced within the ballast layer, whereas the shear stress reaches its maximum value in the subgrade, at 0.6 m below the sleepers, which is the depth chosen for the analysis from Figure 3 (b). It is also important to highlight that the incremental stresses become negligible below a depth of 1.8 m. The above-described stress change patterns agree with past field measurements (Gräbe *et al.*, 2005; Indraratna *et al.*, 2010b; Zhang *et al.*, 2016).

These results may also be interpreted after a stress path plot on $(\sigma_z-\sigma_x)/2$ *vs* τ_{zx} space, which is useful to scrutinise the angle of principal stresses rotation (***α***):

$$2\alpha = \tan^{-1}[2\tau_{zx}/(\sigma_z-\sigma_x)] \qquad (12)$$

The stress paths obtained for a single wheel load present a cardioid pattern consistent with two past studies (*Qian et al., 2016;* Guo *et al.*, 2018), which further validate the benefit of the proposed analytical solution. Notwithstanding, Figure 5 demonstrates how the consideration of multiple axles can transform these cyclic stress paths to become more complex with extra loading-unloading loops. These results are also corroborated by the recent numerical simulations by Zhao *et al.* (2021) and Tucho *et al.* (2022). The rotation angle of the principal stresses along the vertical/longitudinal plane (Eq. 12) is presented in Figure 6. One may observe that the different train loads do not influence this rotation magnitude, which varies from approximately 30° to -30°, however, the higher the train speed, the lesser the time required for one rotation cycle to be completed.

4.2 Jointed rock subgrade

Jointed rock formations are often found in nature containing discontinuities, such as tectonic faults, fractures, natural bedding planes or other planes of weakness, which govern the mechanical behaviour of the rock mass. The discontinuity spatial orientation is described herein according to its strike ($\boldsymbol{\theta_S}$) and dip ($\boldsymbol{\theta_D}$) angles, in relation to the direction of the train movement. The proposed analytical solution considers the strike as the angle (0 to 360°) measured clockwise from the direction of the train movement to the line formed by the intersection of the discontinuity with the horizontal plane. In this convenient definition, a 90° strike is transverse to the track (i.e., perpendicular to the direction of train passage). Correspondingly, the dip is the acute angle (0 to 90°) that the discontinuity makes with the horizontal plane, measured having the plane dipping to the right of the strike direction.

For the present study, the three-dimensional stresses previously calculated for the intact rock subgrade were projected into the perpendicular and tangential directions of the discontinuity plane. Taking the orthogonal unit vectors ***i***, ***j***, and ***k*** respectively along the X, Y, and Z directions (longitudinal in the direction of train passage, transverse and vertical) so that their resultant is the unit vector perpendicular to the discontinuity plane, hence:

$$\mathbf{i} = -\sin(\theta_S).\sin(\theta_D) \tag{13}$$

$$\mathbf{j} = \cos(\theta_S).\sin(\theta_D) \tag{14}$$

$$\mathbf{k} = -\cos(\theta_D) \tag{15}$$

then the normal stress $\boldsymbol{\sigma_n}$ and the shear stress $\boldsymbol{\tau}$ acting on the joint plane can be determined by:

$$\sigma_n = \sigma_x.\mathbf{i}^2 + \sigma_y.\mathbf{j}^2 + \sigma_z.\mathbf{k}^2 + 2\tau_{xz}.\mathbf{i}.\mathbf{k} + 2\tau_{yz}.\mathbf{j}.\mathbf{k} + 2\tau_{xy}.\mathbf{i}.\mathbf{j} \quad (16)$$

$$\tau = [\, (\sigma_x.\mathbf{i} + \tau_{xy}.\mathbf{j} + \tau_{xz}.\mathbf{k})^2 + (\tau_{xy}.\mathbf{i} + \sigma_y.\mathbf{j} + \tau_{yz}.\mathbf{k})^2 + (\tau_{xz}.\mathbf{i} + \tau_{yz}.\mathbf{j} + \sigma_z.\mathbf{k})^2 - \sigma_n^2 \,]^{1/2} \quad (17)$$

For the shear stresses, only the component along the dip direction is assessed, and not the one along the strike direction. This is because we assume that the movement is exclusively along the discontinuity dip direction, as the potential displacement in other directions is constrained by the confinement attributed to the rock blocks and the obvious resistance prevailing along the strike direction.

The discontinuity's normal and shear stresses for Case A, calculated at three depths (0.3, 0.6 and 1.0 m, the same ones for the subgrade without discontinuities) considering three strike angles (0, 45 and 90°) and three dip angles (30, 45 and 60°), are shown in Figure 7. The pattern of the normal and shear stress histories are relatively similar to each other and resemble the one from the orthogonal vertical stress because the magnitude of the latter prevails upon the stresses in the remaining orthogonal directions. One may also appreciate even intuitively that the variation of the discontinuity's dip angle has a greater influence than that of the strike angle, and that is more evident for the normal stress than the shear stress. Albeit the variation of the strike angle exhibits a less apparent influence, the M-shaped history plots for both normal and shear stresses present a slight distortion for higher strikes at z = 0.6 m, more noticeably for the shear stresses. This is because, at such a depth, τ_{xz} reaches its maximum value (see Fig. 6) and thus the effect of principal stresses rotation is more pronounced. Furthermore, the normal and shear stresses along the joint also have their frequencies attenuated with depth, with a pronounced "M" shape for shallower analyses, whilst a single stress pulse from four consecutive axles is observed for greater depths. Figure 7 also includes inserts illustrating the discontinuity's spatial orientation to aid with the interpretation of the results.

Figure 8 presents how the maximum increments of normal and shear stresses vary along the discontinuity length, for Case A and different dip angles. A transverse discontinuity (90° strike) was chosen because the vertical/longitudinal orthogonal shear stress (τ_{xz}) exerts a greater influence under such an orientation. Both normal and shear stresses have their maximum values at the top of the subgrade and are substantially reduced with depth, regardless of the discontinuity's dip angle. The stress increments become negligible below a depth of 1.0 m at the joint with a 30° dip and a depth of 2.0 m at the joint with a 60° dip. The maximum normal stress in Figure 8 (a) is greater at the 30° joint dip and is reduced with the increase of the dip angle, whereas the maximum shear stress in Figure 8 (b) is greater at the 45° joint dip.

The cyclic normal and shear stresses acting on the discontinuity are also assessed following the stress paths presented in Figure 9. Steeper stress paths are observed with an increase in the discontinuity dip and, therefore, closer proximity to the potential strength envelope. It is noteworthy that although the stress increments are higher at the top of the subgrade, the stress paths for deeper layers are more critical (closer to the strength envelope). Furthermore, the linearity of the stress paths or their lack thereof is intrinsically related to the strike angle. When the discontinuity strike is parallel to the track, the shear stress along the dip direction is not influenced by the vertical/longitudinal orthogonal shear stress (τ_{xz}), so the relationship between the normal and shear stresses depends solely on the magnitude of the orthogonal normal stresses. For better clarity, Figure 10 presents a three-dimensional history plot of the normal and shear stresses, in which the stress path pattern is explained by how both stresses vary simultaneously. Note that an increase in the shear stress faster than in the normal stress brings the stress path closer to the potential failure envelope.

In order to assess the influence of the discontinuity spatial orientation, the analysis was extended to study the effect of varying the dip angle continuously from 0 to 90° (from horizontal to vertical) and the strike angle at 15° intervals from 0 to 90° (from parallel to perpendicular to the direction of train passage). Figure 11 presents how the normal and shear stresses vary with the dip and strike angles. As expected, the calculated normal stresses are higher on sub-horizontal discontinuities and become equal to the vertical orthogonal stress (σ_z), whereas they are reduced on sub-vertical joints and become equal to the horizontal orthogonal stresses (σ_y for θ_S=0 and σ_x for θ_S=90). As observed from Figure 11 (a), the variation of strike angles shows that the maximum normal stress is found on a strike of 0° at z=0.3m, whereas on a strike of 90° at the other depths, because $\sigma_y > \sigma_x$ at z=0.3m and $\sigma_y < \sigma_x$ at the other depths (see Figure 4). Regarding the shear stresses, Figure 11 (b) shows that peak values are found on 45° dips and nil values on horizontal and vertical dips for longitudinal strikes (θ_S=0) and equal to the orthogonal shear stress τ_{xz} for transverse strikes (θ_S=90). Inflection points are noticed at dips of 30° and 60° for deeper locations, where the peak shear stress is mobilised on the longitudinal strike instead of the transverse. In the following, two parameters shall be introduced, namely the cyclic normal stress ratio (***CNSR***) and the ratio between the maximum increments of shear and normal stresses (***η***):

$$CNSR = \Delta\sigma_n^{max} / 2p_0 \tag{18}$$

$$\eta = \Delta\tau^{max} / \Delta\sigma_n^{max} \tag{19}$$

where $\boldsymbol{p_0}$ is the mean stress prior to the cyclic load, or the octahedral stress.

For assessing CNSR, a horizontal to vertical initial stress ratio of K = 0.5 was considered conservatively, as for lower values a higher CNSR value is expected. Note that here the magnitude of K is related to the stress ratio prior to cyclic loading, and it does not refer to the conventional *in-situ* earth pressure at rest ($\boldsymbol{K_0}$). For the three cases of train loads under study, Figure 12 presents how CNSR varies with the discontinuity's spatial orientation and depth. The values range up to around 6.5 and are higher for the shallower depth analysis, because of the corresponding lower initial stress state. The pattern of CNSR variation, as expected, is the same as the one for normal stresses from Figure 11 (a), with higher values on sub-horizontal discontinuities and lower values for the sub-vertical discontinuities.

Figure 13 presents the influence of the discontinuity spatial orientation on the shear-to-normal stress ratio. The results are the same for all three cases of train loads because, although the magnitudes of stresses are different for each case, the ratios are still identical. Values of ***η*** are higher for deeper analyses, in which the incremental normal stress is reduced, ranging up to approximately η = 2. The discontinuity dip is more critical around 70° to 80°, increasing the angle for greater depths. Transverse strikes (θ_S = 90°) present more critical values of $\boldsymbol{\eta}$ at z = 0.3 m, whereas for deeper analyses higher values of $\boldsymbol{\eta}$ are obtained for parallel strikes (θ_S = 0°). Possible values of stress ratios for a conventional triaxial lab test ($\boldsymbol{\eta_{triaxial}}$) are also included in Figure 13, emphasizing how these fixed axes (laboratory-type) boundary conditions are capable of emulating moving train loads only for discontinuity dips up to around 30°. For triaxial tests applying a cyclic axial stress $\boldsymbol{\Delta\sigma_a}$ and a constant confining pressure, the normal and shear stresses on the discontinuity, and the respective stress ratio, are obtained as follows:

$$\Delta\sigma_n = \Delta\sigma_a \cdot \cos^2(\theta_D) \tag{20}$$

$$\Delta\tau = \Delta\sigma_a \cdot \sin(\theta_D) \cdot \cos(\theta_D) \tag{21}$$

$$\eta_{\,triaxial} = \sin(\theta_D) \,/\, \cos(\theta_D) \tag{22}$$

As a practical guide, values from Figures 12 and 13 may be adopted for laboratory tests to simulate the load of moving trains more realistically, thus avoiding test conditions with no physical meaning or rare probability of occurrence. Values of CNSR from 1 to 7 and values of η from 0.5 to 2.0 are appropriate starting points for these laboratory tests, in accordance with the inverse relationship presented in Figure 14. In general, higher values of η are related to lower values of CNSR, and vice versa. For instance, a value of η=0.4 should be adopted for a given CNSR=5.0 at z=0.3m from Case A, whilst η=1.2 would correspond to CNSR=0.4 at the same depth and for the same train. For this reason, laboratory testing on rock joints should be able to apply the cyclic normal and shear stress components independently from each other. Furthermore, Figure 14 also elucidates how the CNSR varies for Cases A, B and C, with lower values as the train tonnage is reduced, despite the respective increase in the train speed, whereas η remains unchanged for all three cases.

4.3 Limitations of the analytical solution

For the first step of the analytical solution, the rail is represented by an infinitely long elastic beam supported by a continuously distributed reaction from the ground. Such support is provided along the sleeper width, with no contribution from the crib ballast filling the space between adjoining sleepers. Moreover, the elastic beam is assumed to be subjected exclusively to vertical forces and moments, which is a valid assumption to determine ground stresses generated by the train vertical load. Horizontal forces and/or torque caused by train acceleration/deceleration, temperature changes, effects of differential settlements and sleeper movements along the track, among others, are thus neglected. The present analytical solution calculates dynamic stresses after multiplying the train static load by a dynamic amplification factor (DAF), however, impact forces such as those caused by wheel imperfections and rail corrugations (Indraratna *et al.*, 2010b) are not considered.

The vertical pressure underneath each sleeper is then assumed as uniformly distributed on a rectangular area equivalent to the outer thirds of the sleeper base, as the second step of the analytical solution. Although the real stress distribution along the sleeper length (transverse to the track) is not captured, the comparison of calculated stresses and field measurements demonstrates how the analytical prediction is more accurate immediately beneath the sleepers than with depth (see Figure 2 c).

As the third step of this analytical solution, the distribution of stresses in the ground is then calculated using Boussinesq elastic solution. The relevant equations are based on the assumption of a homogenous and isotropic, linearly elastic (infinite half-space) ground. For a jointed rock subgrade, which is the main objective of this study, the Boussinesq solution could be extended to consider the anisotropy of the rock mass (Willis, 1967). However, the integration of such an anisotropic solution across the rectangular area underneath the sleepers cannot be worked out explicitly and would require resorting to calculations with computational iterations. Alternatively, numerical simulations using Finite Elements or Distinct Elements methods can be used to understand the stress and deformation responses of anisotropic rock masses, as suggested by Deng et al. (2021).

As reported in previous studies (Jaeger and Cook, 1979; Tonon and Amadei, 2005; Mehranpour et al. 2018; Renani et al., 2019), the strength and deformation modulus of an anisotropic rock mass change with the orientation and spacing of the joints with respect to the loading direction (*i.e.*, vertical in this study). Although the ground reaction coefficient (k) considered in this study encompasses the influence of the anisotropic jointed rock mass as the subgrade, for simplicity, its value is kept constant for variable joint orientations.

Finally, the stresses acting along the joints are obtained by projecting the orthogonal stresses onto the joint plane. This means that they refer to the situation immediately after the load is applied, *i.e.* prior to any joint response. As the joint normal and shear displacements take place and its frictional resistance is mobilised, the surrounding stresses in the rock matrix become redistributed. Even more so in the case when the joint strength is reached, because, the shear stress cannot be increased further, and the redistribution of stresses then becomes more pronounced.

The present analytical solution, nevertheless, does not capture the joint response because only the stresses are calculated, and not the displacements. As observed in Figure 9, the stress paths are closer to the joint strength envelope (friction angle of 40°) for the analyses at z=0.6m and as the joint strike angle is increased (Fig. 9e and 9f). If the joint considered in this study had a lower friction angle, the stress paths would cross beyond the strength envelope. In this case, the design of the track structure would need to be reviewed and improved."

5. Conclusions

An analytical solution was proposed to calculate the incremental stresses stemming from moving train loads. Not only is its validation against field measurements and numerical simulations adequate, but also corroborates that this is an effective, powerful tool, with strong practical appeal for the rail industry.

The solution is able to estimate the complete three-dimensional incremental stresses in the ground, as well as their variation with depth and along the train passage direction, under the influence of multiple axles from the train composition. The study demonstrated that a conservative design is rendered when the increment of vertical stress is considered solely, as the deviator stress is overestimated, and that in this case the principal stresses rotation typically caused by moving loads is not captured properly.

The results of this study indicated that the variation of stresses with depth exposed how the critical stress state would not necessarily take place at shallower depths where the vertical stress was higher, but rather where the incremental shear stress was maximum (i.e., z=0.60 for the present study).

The study revealed that there is a change in the pattern of stress histories once discontinuities are considered in the rock subgrade. The incremental normal and shear stresses acting on the discontinuity plane, calculated using the proposed analytical solution, had different magnitudes yet practically the same curve pattern, which resembled the one from the vertical orthogonal stress. Additionally, such stress-history curves were in phase with each other, *i.e.* their peak values were aligned in time. Such a pattern is not found for homogeneous grounds, without discontinuities.

Although the magnitudes of normal and shear stresses may vary according to the train load and speed, as well as to the discontinuity's spatial orientation, the paper elucidated that their relation to the initial stress state and each other, i.e. the cyclic normal stress ratio (*CNSR*) and the shear-to-normal stress ratio (η), present a limited range of possible, practical values. According to the results herein obtained, to simulate loads from moving trains adequately, laboratory tests on rock joints should be able to apply cyclic normal and shear stresses independently from each other and, notwithstanding, with CNSR and η values following an inverse relationship and limited within the ranges of **CNSR = 1 to 7** and **η = 0.5 to 2.0**.

This study demonstrated that conventional triaxial tests would not be capable of applying normal and shear stresses independently of each other on a joint, therefore they could only emulate moving train loads for dip angles up to around 30°. In contrast, direct shear and ring shear equipment could be adapted with two dynamic attenuators installed in opposite horizontal directions and one in the vertical direction, whilst simple shear and hollow cylinder apparatuses are usually capable of applying cyclic normal and shear forces/displacements independently.

Appendix

The incremental vertical stress $\boldsymbol{\Delta\sigma_z}$ for points of interest along the vertical projection of the corner of a uniformly loaded rectangular area is calculated, after the integration of Boussinesq's solution by Newmark (1935), as:

$$\Delta\sigma_z = P \, . \, I_{f,\,z} = \frac{P}{4\pi}\left[\frac{\left(2\,m\,n\,\sqrt{m^2+n^2+1}\right)\left(m^2+n^2+2\right)}{\left(m^2+n^2+m^2n^2+1\right)\left(m^2+n^2+1\right)} + \tan^{-1}\left(\frac{2\,m\,n\,\sqrt{m^2+n^2+1}}{m^2+n^2-m^2n^2+1}\right)\right] \quad \text{(A1)}$$

$$m = x/z \text{ and } n = y/z \quad \text{(A2)}$$

where $\boldsymbol{I_f}$ is the influence factor that multiplies the vertical pressure $\boldsymbol{P}$ applied by the sleeper, $\boldsymbol{x}$ and $\boldsymbol{y}$ are the length and width of the loaded area, respectively, and $\boldsymbol{z}$ is the depth of the point below the corner of this loaded area at which the stress is being calculated.

The incremental stresses in the remaining directions, i.e. the horizontal longitudinal and transverse stresses, $\boldsymbol{\Delta\sigma_x}$ and $\boldsymbol{\Delta\sigma_y}$, and shear stresses on the vertical/longitudinal, vertical/transverse and horizontal planes, respectively $\boldsymbol{\Delta\tau_{xz}}$, $\boldsymbol{\Delta\tau_{yz}}$, and $\boldsymbol{\Delta\tau_{xy}}$, are calculated for the same boundary conditions after the integration of Boussinesq's solution by Holl (1940) as:

$$\Delta\sigma_x = P \, . \, I_{f,\,x} = \frac{P}{2\pi}\left[\tan^{-1}\left(\frac{x\,y}{z\sqrt{x^2+y^2+z^2}}\right) - \frac{x\,y\,z}{\left(x^2+z^2\right)\sqrt{x^2+y^2+z^2}}\right] \quad \text{(A3)}$$

$$\Delta\sigma_y = P\ .\ I_{f,\,y} = \frac{P}{2\pi}\left[\tan^{-1}\left(\frac{x\,y}{z\sqrt{x^2+y^2+z^2}}\right)-\frac{x\,y\,z}{(y^2+z^2)\sqrt{x^2+y^2+z^2}}\right] \tag{A4}$$

$$\Delta\tau_{xz} = P\ .\ I_{f,\,xz} = \frac{P}{2\pi}\left(\frac{y}{\sqrt{y^2+z^2}}-\frac{y\,z^2}{(x^2+z^2)\sqrt{x^2+y^2+z^2}}\right) \tag{A5}$$

$$\Delta\tau_{yz} = P\ .\ I_{f,\,yz} = \frac{P}{2\pi}\left(\frac{x}{\sqrt{x^2+z^2}}-\frac{x\,z^2}{(y^2+z^2)\sqrt{x^2+y^2+z^2}}\right) \tag{A6}$$

$$\Delta\tau_{xy} = P\ .\ I_{f,\,xy} = \frac{P}{2\pi}\left[1+\frac{z}{\sqrt{x^2+y^2+z^2}}-z\left(\frac{1}{\sqrt{x^2+z^2}}-\frac{1}{\sqrt{y^2+z^2}}\right)\right] \tag{A7}$$

Frazee (2021) further explained that the stresses $\boldsymbol{\Delta\sigma_x}$, $\boldsymbol{\Delta\sigma_y}$, and $\boldsymbol{\Delta\tau_{xy}}$ depend on the Poisson's ratio $\boldsymbol{v}$ in the original Boussinesq's equations and that the terms multiplied by $(1 - 2v)$ do not integrate cleanly. That is why the solution by Holl (1940) was derived using **$v = 0.50$** (i.e. no volume change / undrained) so that such term is zeroed. Giroud (1970) continued Holl's work and tabulated $\boldsymbol{I_f}$ values for $\boldsymbol{\Delta\sigma_x}$ and $\boldsymbol{\Delta\sigma_y}$ that take into account different values of Poisson's ratio. But alas, shear stresses are not contemplated and the tables present very limited values of depths and dimensions of the rectangular loaded area.

Bearing in mind that this solution is linear, the contribution of adjacent sleepers is accounted for considering the principle of superposition, thus the incremental stresses $\boldsymbol{\Delta}$ under the rail alignment are obtained as:

$$\Delta = \ldots + 2.P_{n-1}.[I_f^{(+)}{}_{n-1} - I_f^{(-)}{}_{n-1}] + 4.P_n.I_{f,\,n} + 2.P_{n+1}.[I_f^{(+)}{}_{n+1} - I_f^{(-)}{}_{n+1}] + \ldots \tag{A8}$$

where $\boldsymbol{n}$ is the sleeper number, $\boldsymbol{I_f^{(+)}}$ is the influence factor calculated for the loaded areas and $\boldsymbol{I_f^{(-)}}$ is the factor calculated for the areas outside the footprint of the loaded area, as illustrated in Figure A1. Normally, two up to five adjacent sleepers in each direction must be accounted for, depending on the width of the rail reaction curve. For points of interest beneath the rail alignment, the incremental shear stresses on the vertical/transverse plane (τ_{yz}) and on the horizontal plane (τ_{xy}) are null due to the load symmetry.

Data availability statement

Some or all data used are available from the corresponding author by request.

Acknowledgements

This study was conducted under the auspices of the Industrial Transformation Training Centre for Advanced Technologies in Rail Track Infrastructure (ITTC-Rail), c/o Australian Research Council (ARC-IC170100006). This work was partially inspired by Prof ET (Ted) Brown as a result of his long-term collaboration with Prof Buddhima Indraratna in the field of jointed rock engineering, prior to his total retirement a few years ago. The authors gratefully appreciate the close collaborations with SMEC (c/o Dr Richard Kelly) for valuable inputs and help throughout the project. The first author is also grateful to Dr Ameyu Temesgen Tucho for the fruitful discussions about the topic.

References

AREMA, American Railway Engineering and Maintenance-of-Way Association (2019). *Manual for Railway Engineering*, Washington.

ARTC, Australian Rail Track Corporation Limited (2022). *Route access standard - General information*, version 2.4, 71p. Available at: http://www.artc.com.au/customers/standards/route/access.

BARBERO, M., BARLA, G. and ZANINETTI, A. (1996). Dynamic shear strength of rock joints subjected to impulse loading, *International Journal of Rock Mechanics and Mining Sciences & Geomechanics Abstracts*, **33**(2), pp.141-151, DOI: 10.1016/0148-9062(95)00049-6.

BATHURST, L.A. and KERR, A.D. (1999). An improved analysis for the determination of required ballast depth, *Proceedings* of AREMA, Chicago, 32p.

BERTUZZI, R. (2016). Strength and stiffness properties of defects within the Hawkesbury Sandstone and Ashfield Shale, *Australian Geomechanics Journal*, **51**(3), pp.693-101.

BIAN, X., LI, W., QIAN, Y. and TUTUMLUER, E. (2020). Analysing the effect of principal stress rotation on railway track settlement by discrete element method, *Géotechnique*, **70**(9), pp.803-821, DOI: 10.1680/jgeot.18.P.368.

BOUSSINESQ, J. (1883). *Application des potentials à l'etude de l'equilibre et du movement des solides elastiques*, Paris: Gauthier-Villars.

BROWN, S.F. (1996). Soil mechanics in pavement engineering, *Géotechnique*, **46**(3), pp.383-426, DOI: 10.1680/geot.1996.46.3.383.

CASAGRANDE, D., BUZZI, O., GIACOMINI, A., LAMBERT, C. and FENTON, G. (2018). A new stochastic approach to predict peak and residual shear strength of natural rock discontinuities, *Rock Mechanics and Rock Engineering*, **51**(1), pp.69-99, DOI: 10.1007/s00603-017-1302-3.

COLAÇO, A., COSTA, P.M.B.A. and LOPES, P. (2015). Análise numérica da alteração do estado de tensão geomecânico induzida pelo tráfego ferroviário, *Revista Internacional de Métodos Numéricos para Cálculo y Diseño en Ingeniería*, **31**(2), pp.120-131, DOI: 10.1016/j.rimni.2014.02.001.

COSTA, P.M.B.A. (2011). Vibrações do sistema via-maciço induzidas por tráfego ferroviário: modelação numérica e validação experimental. Thesis (PhD), Universidade do Porto, 436p. Available at: http://hdl.handle.net/10216/61470.

DANG, W., KONIETZKY, H. and FRÜHWIRT, T. (2016). Direct shear behavior of a plane joint under dynamic normal load (DNL) conditions, *Engineering Geology*, **213**, pp.133-141, DOI: 10.1016/j.enggeo.2016.08.016.

DANG, W., KONIETZKY, H., CHANG, L. and FRÜHWIRT, T. (2018). Velocity-frequency-amplitude-dependent frictional resistance of planar joints under dynamic normal load (DNL) conditions, *Tunnelling and Underground Space Technology*, **79**, pp.27-34, DOI: 10.1016/j.tust.2018.04.038.

DENG, P., LIU, Q., HUANG, X., PAN, Y. and WU, J. (2022). FDEM numerical modeling of failure mechanisms of anisotropic rock masses around deep tunnels, *Computers and Geotechnics*, **142**, p.104535. DOI: 10.1016/j.compgeo.2021.104535.

ESEN, A.F., WOODWARD, P.K., LAGHROUCHE, O. and CONNOLLY, D.P. (2022). Stress distribution in reinforced railway structures, *Transportation Geotechnics*, **32**, p.100699, DOI: 10.1016/j.trgeo.2021.100699.

ESVELD, C. (2001). *Modern railway track*, 2nd edition edn, The Netherlands, ISBN: 9080032433.

FATHI, A., MORADIAN, Z., RIVARD, P. and BALLIVY, G. (2016). Shear mechanism of rock joints under pre-peak cyclic loading condition, *International Journal of Rock Mechanics and Mining Sciences*, **83**, pp.197-210, DOI: 10.1016/j.ijrmms.2016.01.009.

FRAZEE, G.R. (2021). New formulations of Boussinesq solution for vertical and lateral stresses in soil, *Practice Periodical on Structural Design and Construction*, **26**(2), 12 p, DOI: 10.1061/(ASCE)SC.1943-5576.0000567.

GIROUD, J.P. (1970). Stresses under linearly loaded rectangular area, *Journal of the Soil Mechanics and Foundations Division*, **96**(1), pp.263-268, DOI: 10.1061/JSFEAQ.0001386.

GRÄBE, P.J., CLAYTON, C.R.I. and SHAW, F.J. (2005). Deformation measurement on a heavy haul track formation, *Proceedings* of 8th International Heavy Haul Conference, Rio de Janeiro - Brazil: International Heavy Haul Association, pp.287-295.

GUO, L., CAI, Y., JARDINE, R.J., YANG, Z. and WANG, J. (2018). Undrained behaviour of intact soft clay under cyclic paths that match vehicle loading conditions, *Canadian Geotechnical Journal*, **55**(1), pp.90-106, DOI: 10.1139/cgj-2016-0636.

HAN, Z.L. and ZHANG, Q.L. (2005). Dynamic stress analysis on speed increase subgrade of existing railway, *China Railway Science*, **26**(5), pp.1-5.

HOLL, D.L. (1940). Stress transmission in earths, *Proceedings* of High. Res. Board, v.20, pp.709-721.

HSIUNG, S.M., GHOSH, A., CHOWDHURY, A.H. and AHOLA, M.P. 1993, *Evaluation of rock joint models and computer code UDEC against experimental results*, Nuclear Regulatory Commission, Washington DC, CNWRA 93-024.

HSIUNG, S.M., KANA, D.D., AHOLA, M.P., CHOWDHURY, A.H. and GHOSH, A. 1994, *Laboratory characterization of rock joints*, Nuclear Regulatory Commission, Washington DC, CNWRA 93-013.

INDRARATNA, B., SALIM, W. and RUJIKIATKAMJORN, C. (2011). *Advanced Rail Geotechnology - Ballasted Track*, The Netherlands: CRC Press/Balkema, 432p, ISBN: 9781138072893.

INDRARATNA, B., NIMBALKAR, S. and NEVILLE, T. (2014). Performance assessment of reinforced ballasted rail track, *Proceedings of the Institution of Civil Engineers - Ground Improvement*, **167**(1), pp.24-34, DOI: 10.1680/grim.13.00018.

INDRARATNA, B., SOOMRO, M.H.A.A. and RUJIKIATKAMJORN, C. (2021). Semi-empirical analytical modelling of equivalent dynamic shear strength (EDSS) of rock joint, *Transportation Geotechnics*, **29**, p.100569, DOI: 10.1016/j.trgeo.2021.100569.

INDRARATNA, B., OLIVEIRA, D.A.F., BROWN, E.T. and ASSIS, A.P. (2010a). Effect of soil–infilled joints on the stability of rock wedges formed in a tunnel roof, *International Journal of Rock Mechanics and Mining Sciences*, **47**(5), pp.739-751, DOI: 10.1016/j.ijrmms.2010.05.006.

INDRARATNA, B., NIMBALKAR, S., CHRISTIE, D., RUJIKIATKAMJORN, C. and VINOD, J. (2010b). Field assessment of the performance of a ballasted rail track with and without geosynthetics, *Journal of Geotechnical and Geoenvironmental Engineering*, **136**(7), pp.907-917, DOI: 10.1061/(ASCE)GT.1943-5606.0000312.

JAEGER, J.C. and COOK, N.G.W. (1979). *Fundamentals of Rock Mechanics*, 3rd edition, London: Chapman and Hall, 593p.

JAFARI, M.K., AMINI HOSSEINI, K., PELLET, F., BOULON, M. and BUZZI, O. (2003). Evaluation of shear strength of rock joints subjected to cyclic loading, *Soil Dynamics and Earthquake Engineering*, **23**(7), pp.619-630, DOI: 10.1016/S0267-7261(03)00063-0.

JEFFERY, M., CRUMPTON, M., FITYUS, S.G., HUANG, J., GIACOMINI, A. and BUZZI, O. (2022). A shear device with controlled boundary conditions for very large nonplanar rock discontinuities, *Geotechnical Testing Journal*, **45**(4), pp.725-752, DOI: 10.1520/GTJ20210220.

JEFFS, T. and TEW, G.P. (1991). *A Review of Track Design Procedures: Sleepers and ballast*, vol. 2, Melbourne: Railways of Australia BHP Research, 205p, ISBN: 9780909582036.

KANDAUROV, I.I. (1966). *Mechanics of discrete media and its application to construction* Leningrad, Russia: Liter Po Stroitel'stvu.

LAMAS-LOPEZ, F., CUI, Y.-J., CALON, N., D'AGUIAR, S.C., OLIVEIRA, M.P. and ZHANG, T. (2016). Track-bed mechanical behaviour under the impact of train at different speeds, *Soils and Foundations*, **56**(4), pp.627-639, DOI: 10.1016/j.sandf.2016.07.004.

LI, D. and SELIG, E.T. (1998). Method for Railroad Track Foundation Design. II: Applications, *Journal of Geotechnical and Geoenvironmental Engineering*, **124**(4), pp.323-329, DOI: 10.1061/(ASCE)1090-0241(1998)124:4(323).
LI, Z.C. (2000). Study on the vertical load transmission through the track structure and the characteristics of subgrade dynamic stresses. Thesis (PhD), China Academy of Railway Sciences, Beijing, China.
LIU, J. and XIAO, J. (2010). Experimental study on the stability of railroad silt subgrade with increasing train speed, *Journal of Geotechnical and Geoenvironmental Engineering*, **136**(6), pp.833-841, DOI: 10.1061/(ASCE)GT.1943-5606.0000282.
LIU, M. and LIU, E. (2017). Dynamic mechanical properties of artificial jointed rock samples subjected to cyclic triaxial loading, *International Journal of Rock Mechanics and Mining Sciences*, **98**, pp.54-66, DOI: 10.1016/j.ijrmms.2017.07.005.
LIU, Y. and DAI, F. (2018). A damage constitutive model for intermittent jointed rocks under cyclic uniaxial compression, *International Journal of Rock Mechanics and Mining Sciences*, **103**, pp.289-301, DOI: 10.1016/j.ijrmms.2018.01.046.
MAROLT ČEBAŠEK, T., ESEN, A.F., WOODWARD, P.K., LAGHROUCHE, O. and CONNOLLY, D.P. (2018). Full scale laboratory testing of ballast and concrete slab tracks under phased cyclic loading, *Transportation Geotechnics*, **17**, pp.33-40, DOI: 10.1016/j.trgeo.2018.08.003.
MASSEY, F.J. (1951). The Kolmogorov-Smirnov test for goodness of fit, *Journal of the American Statistical Association*, **46**(253), pp.68-78, DOI: 10.2307/2280095.
MEHRANPOUR, M.H., KULATILAKE, P.H.S.W., XINGEN, M. and HE, M. (2018). Development of new three-dimensional rock mass strength criteria, *Rock Mechanics and Rock Engineering*, **51**(11), pp.3537-3561. DOI: 10.1007/s00603-018-1538-6.
MOMOYA, Y., SEKINE, E. and TATSUOKA, F. (2005). DEFORMATION CHARACTERISTICS OF RAILWAY ROADBED AND SUBGRADE UNDER MOVING-WHEEL LOAD, *SOILS AND FOUNDATIONS*, **45**(4), pp.99-118, DOI: 10.3208/sandf.45.4_99.
NEWMARK, N.M. (1935). Simplified computation of vertical pressure in elastic foundations. Thesis (Circular 24), University of Illinois Engineering Experiment Station.
NIE, Z., RUAN, B. and LI, L. (2005). Dynamic test and analysis of subgrade structure in cutting section of Qinshen passenger dedicated line, *Vibration and Shock*, **24**(2), pp.30-32.
NIMBALKAR, S. and INDRARATNA, B. (2016). Improved performance of ballasted rail track using geosynthetics and rubber shockmat, *Journal of Geotechnical and Geoenvironmental Engineering*, **142**(8), 13 p, DOI: 10.1061/(ASCE)GT.1943-5606.0001491.
NIMBALKAR, S., INDRARATNA, B., DASH, S.K. and CHRISTIE, D. (2012). Improved performance of railway ballast under impact loads using shock mats, *Journal of Geotechnical and Geoenvironmental Engineering*, **138**(3), pp.281-294, DOI: 10.1061/(ASCE)GT.1943-5606.0000598.
ODEMARK, N. 1949, *Undersökning av elasticitetsegenskaperna hos olika jordarter samt teori för beräkning av beläggningar enligt elasticitetsteorin*, 00815713 (ISSN), Statens Väginstitut, Stockholm, 77.

PEELLAGE, W.H., FATAHI, B. and RASEKH, H. (2022). Experimental investigation for vibration characteristics of jointed rocks using cyclic triaxial tests, *Soil Dynamics and Earthquake Engineering*, **160**, p.107377, DOI: 10.1016/j.soildyn.2022.107377.

PELLS, P.J.N. (2004). Substance and mass properties for the design of engineering structures in the Hawkesbury Sandstone, *Australian Geomechanics Journal*, **39**(3), 21p.

POWRIE, W., YANG, L.A. and CLAYTON, C.R.I. (2007). Stress changes in the ground below ballasted railway track during train passage, *Proceedings of the Institution of Mechanical Engineers, Part F: Journal of Rail and Rapid Transit*, **221**(2), pp.247-262, DOI: 10.1243/0954409jrrt95.

POWRIE, W., LE PEN, L., MILNE, D. and THOMPSON, D. (2019). Train loading effects in railway geotechnical engineering: Ground response, analysis, measurement and interpretation, *Transportation Geotechnics*, **21**, p.100261, DOI: 10.1016/j.trgeo.2019.100261.

PRIEST, J.A., POWRIE, W., YANG, L., GRÄBE, P.J. and CLAYTON, C.R.I. (2010). Measurements of transient ground movements below a ballasted railway line, *Géotechnique*, **60**(9), pp.667-677, DOI: 10.1680/geot.7.00172.

QIAN, J.-G., WANG, Y.-G., YIN, Z.-Y. and HUANG, M.-S. (2016). Experimental identification of plastic shakedown behavior of saturated clay subjected to traffic loading with principal stress rotation, *Engineering Geology*, **214**, pp.29-42, DOI: 10.1016/j.enggeo.2016.09.012.

RENANI, H.R., MARTIN, C.D. and CAI, M. (2019). An analytical model for strength of jointed rock masses, *Tunnelling and Underground Space Technology*, **94**, p.103159. DOI: 10.1016/j.tust.2019.103159.

SCHWEDLER, J.W. (1882). On iron permanent way, *Proceedings* of the Institution of Civil Engineers, v.67, n.1, London: ICE, pp.95-118. DOI: 10.1680/imotp.1882.21993.

SHENTON, M.J. (1975). Deformation of railway ballast under repeated loading conditions, *Proceedings* of Railroad Track Mechanics and Technology, ed. A.D. Kerr, Princeton University, pp.387-404.

SOOMRO, M.H.A.A., INDRARATNA, B. and KAREKAL, S. (2022). Critical shear strain and sliding potential of rock joint under cyclic loading, *Transportation Geotechnics*, **32**, p.100708, DOI: 10.1016/j.trgeo.2021.100708.

SUN, Q.D., INDRARATNA, B. and NIMBALKAR, S. (2016). Deformation and degradation mechanisms of railway ballast under high frequency cyclic loading, *Journal of Geotechnical and Geoenvironmental Engineering*, **142**(1), p.04015056,12 p, DOI: 10.1061/(ASCE)GT.1943-5606.0001375.

THIRUKUMARAN, S., INDRARATNA, B., BROWN, E.T. and KAISER, P.K. (2016). Stability of a rock block in a tunnel roof under constant normal stiffness conditions, *Rock Mechanics and Rock Engineering*, **49**(4), pp.1587-1593, DOI: 10.1007/s00603-015-0770-6.

TONON, F. and AMADEI, B. (2003). Stresses in anisotropic rock masses: an engineering perspective building on geological knowledge, *International Journal of Rock Mechanics and Mining Sciences*, **40**(7), pp.1099-1120. DOI: 10.1016/j.ijrmms.2003.07.009.

TUCHO, A., INDRARATNA, B. and NGO, T. (2022). Stress-deformation analysis of rail substructure under moving wheel load, *Transportation Geotechnics*, **36**, p.100805, DOI: 10.1016/j.trgeo.2022.100805.

WANG, G., ZHANG, X., JIANG, Y., WU, X. and WANG, S. (2016). Rate-dependent mechanical behavior of rough rock joints, *International Journal of Rock Mechanics and Mining Sciences*, **83**, pp.231-240, DOI: 10.1016/j.ijrmms.2015.10.013.

WANG, H., ZENG, L.-L., BIAN, X. and HONG, Z.-S. (2020). Train moving load-induced vertical superimposed stress at ballasted railway tracks, *Advances in Civil Engineering*, vol.2020, 11 p, DOI: 10.1155/2020/3428395.

WILLIS, J.R. (1967). Boussinesq problems for an anisotropic half-space, *Journal of the Mechanics and Physics of Solids*, **15**(5), pp.331-339. DOI: 10.1016/0022-5096(67)90027-0.

XU, F., YANG, Q., LIU, W., LENG, W., NIE, R. and MEI, H. (2018). Dynamic stress of subgrade bed layers subjected to train vehicles with large axle loads, *Shock and Vibration*, **2018**, 12 p, DOI: 10.1155/2018/2916096.

YANG, L.A., POWRIE, W. and PRIEST, J.A. (2009). Dynamic stress analysis of a ballasted railway track bed during train passage, *Journal of Geotechnical and Geoenvironmental Engineering*, **135**(5), pp.680-689, DOI: 10.1061/(ASCE)GT.1943-5606.0000032.

ZHANG, T.W., CUI, Y.J., LAMAS-LOPEZ, F., CALON, N. and COSTA D'AGUIAR, S. (2016). Modelling stress distribution in substructure of French conventional railway tracks, *Construction and Building Materials*, **116**, pp.326-334, DOI: 10.1016/j.conbuildmat.2016.04.137.

ZHAO, H.Y., INDRARATNA, B. and NGO, T. (2021). Numerical simulation of the effect of moving loads on saturated subgrade soil, *Computers and Geotechnics*, **131**, p.103930, DOI: 10.1016/j.compgeo.2020.103930.

ZHAO, X. (2011). Study on the assessment theory and measures of subgrade quality of Datong-Qinhuangdao heavy load railway. Thesis (MSc), Beijing Jiaotong University, Beijing, China.

Figure captions

Figure 1. Flowchart with the calculation sequence.

Figure 2. Validation of the analytical solution: (a) σ_{calc} versus σ_{ref}, (b) cumulative probability of occurrence of $\sigma_{calc}/\sigma_{ref}$, and (c) variation of $\sigma_{calc}/\sigma_{ref}$ with depth.

Figure 3. Stresses calculated for three wagons of Case A train, at the depths (a) 0.30 m, (b) 0.60 m, and (c) 1.0 m.

Figure 4. Variation of maximum stresses with depth for (a) Case A, (b) Case B, and (c) Case C.

Figure 5. Cyclic stress paths for (a) Case A, (b) Case B, and (c) Case C.

Figure 6. Major and minor principal stresses rotation angles for (a) Case A, (b) Case B, and (c) Case C.

Figure 7. Normal and shear stresses on the discontinuity for Case A train at (a) (b) (c) z=0.3m, (d) (e) (f) z=0.6m, and (g) (h) (i) z=1.0m, with variable dip angles and (a) (d) (g) strike=0°, (b) (e) (h) strike=45°, and (c) (f) (i) strike=90°.

Figure 8. Variation of (a) maximum normal stress and (b) maximum shear stress along the joint length for Case A train, with strike=90° (transverse) and dip angles=30°, 45° and 60°.

Figure 9. Cyclic stress paths on the discontinuity for Case A train at (a) (b) (c) z=0.3m, (d) (e) (f) z=0.6m, and (g) (h) (i) z=1.0m, with variable dip angles and (a) (d) (g) strike=0°, (b) (e) (h) strike=45°, and (c) (f) (i) strike=90°.

Figure 10. Cyclic stress path on the discontinuity for Case A train at the top of the subgrade (z=0.3m), for strike=90° (transverse) and dip=45°.

Figure 11. Influence of the discontinuity spatial orientation on the (a) normal stress and (b) shear stress, for Case A train and different depths.

Figure 12. Influence of the discontinuity spatial orientation on the cyclic normal stress ratio for three different depths and (a) Case A, (b) Case B and (c) Case C.

Figure 13. Influence of the discontinuity spatial orientation on the shear-to-normal stress ratio for the depths (a) z=0.3m, (b) z=0.6m and (c) z=1.0m, for Cases A, B and C (identical η for the three cases).

Figure 14. Relation between CNSR and η for different depths, discontinuity strikes and for (a) Case A, (b) Case B and (c) Case C.

Figure A1. Plan view illustration of the superposition process to account for the influence of adjacent sleepers.

Table captions

Table 1. List of case studies and ground properties.

Table 2. Input parameters and results of the analyses carried out for all case studies.

Table 1. List of case studies and ground properties.

Case	Site	Layers				k	Reference
		thickness (m)	E (MPa)	ν	K_0	(MN/m^2)	
1 [F]	Bulli, Australia	0.30 ballast	250	0.30		90	Indraratna *et al.* (2010), Nimbalkar *et al.* (2012)
		0.15 capping	50	0.30			
		subgrade (silty clay)	30	0.30			
2 [F]	Singleton, Australia	0.30 ballast	300	0.30		90	Indraratna *et al.* (2014), Nimbalkar & Indraratna (2016)
		0.15 sub-ballast	200	0.30			
		0.50 structural fill	100	0.30			
		0.80 general fill	70	0.30			
		subgrade (silty clay)	10	0.30			
3 [F]	Singleton, Australia	0.30 ballast			0.90	150	
		0.15 sub-ballast			0.80		
		0.50 structural fill			0.60		
		0.15 transition			0.60		
		subgrade (siltstone)			0.45		
4 [F]	Vierzon, France	0.50 ballast	250	0.30		80	Lamas-Lopez *et al.* (2016), Zhang *et al.* (2016)
		0.40 interlayer	200	0.30			
		0.20 transition	150	0.30			
		subgrade (silty sand)	30	0.30			
5 [F]	Bloubank, South Africa	0.30 ballast			0.80	100	Gräbe *et al.* (2005)
		0.80 structural fill			0.60		
		subgrade (mudstone)			0.45		
6 [F]	Jian-Qingdao, China	0.25 ballast	200	0.30		20	Liu & Xiao (2010)
		0.20 capping	150	0.30			
		subgrade (silt)	20	0.30			
7 [F]	Tianjin-Pukou, China	0.25 ballast	200	0.30		20	
		0.40 capping	150	0.30			
		subgrade (silt)	20	0.30			
8 [F]	Guangzhou-Shenzhen, China	0.45 ballast	200	0.30		30	Li (2000) *apud* Wang *et al.* (2020)
		subgrade (soil)	30	0.30			
9 [F]	Haerbin-Beian, China	0.40 ballast			0.80	120	
		subgrade (rock)			0.60		
10 [F]	Hangzhou-Nanchang, China	0.40 ballast			0.80	150	
		subgrade (rock)			0.60		
11 [F]	Zhejiang-Ganxi, China	0.40 ballast	200	0.30		70	Han & Zhang (2005)
		subgrade (soil)	145	0.30			
12 [F]	Beijing, China	0.35 ballast	200	0.30		10	
		subgrade (soil)	15	0.30			
13 [F]	Xiaoshan-Ningbo, China	0.45 ballast	200	0.30		40	
		subgrade (soil)	60	0.30			
14 [F]	Qin-Shen, China	0.40 ballast			0.90	100	Nie *et al.* (2005)
		0.40 structural fill			0.80		
		subgrade (granite)			0.40		
15 [F]	Da-Qin, China	0.45 ballast	200	0.30		20	Zhao (2011) *apud* Wang *et al.* (2020)
		1.00 structural fill	150	0.30			
		subgrade (soil)	20	0.30			
16 [L]	full-scale lab test, China	0.40 ballast			0.70	200	Bian *et al.* (2020)
		0.70 sub-ballast			0.60		
		2.05 embankment			0.50		
		subgrade (reaction slab)			0.40		
17 [L]	full-scale lab test, UK	0.40 ballast			0.90	200	Esen *et al.* (2022), Marolt Čebašek *et al.* (2018)
		0.40 frost protection			0.80		
		0.80 embankment			0.70		
		subgrade (reaction slab)			0.40		
18 [N]	Vryheid, South Africa	0.30 ballast			0.80	100	Yang *et al.* (2009), Priest *et al.* (2010)
		0.80 structural fill			0.60		
		subgrade (mudstone)			0.45		

19 [N]	Carregado, Portugal	0.35 ballast	97	0.12	70	Costa (2011), Colaço *et al.* (2015)
		0.55 sub-ballast	212	0.30		
		subgrade (silty clay)	127.4	0.40		
20 [N]	Hebei, China	0.50 ballast	200	0.25	40	Xu *et al.* (2018)
		0.60 top sub-ballast	180	0.30		
		1.90 bottom sub-ballast	150	0.30		
		3.00 embankment	70	0.35		
		subgrade (clay)	50	0.35		
21 [N]	Bulli, Australia	0.30 ballast	200	0.30	90	Tucho *et al.* (2022)
		0.15 capping	150	0.30		
		subgrade (silty clay)	50	0.35		

Notes: [F] = field measurements cases; [L] = lab tests cases; [N] = numerical analyses cases

Table 2. Input parameters and results of the analyses carried out for all case studies.

Case		Train axle (t)	Train V (km/h)	Rail E (GPa)	Rail I ($10^{-5}m^4$)	Sleepers L (m)	Sleepers B (m)	Sleepers S (m)	Analysis depth below sleeper (m)	σ_{calc} (kPa)	σ_{ref} (kPa)
1	1.1	25	60	210	3.055	2.50	0.26	0.60	0 (sleeper/ballast)	259.6	255
									0.30 (ballast/capping)	66.7	70
									0.45 (capping/subgrade)	50.9	55
	1.2	20.5	60						0 (sleeper/ballast)	176.5	175
									0.30 (ballast/capping)	45.3	39
									0.45 (capping/subgrade)	34.6	32
2	2.1	25	40	210	3.055	2.50	0.26	0.60	0 (sleeper/ballast)	252.4	250
									0.30 (ballast/sub-ballast)	40.6	35
	2.2	25	80						0 (sleeper/ballast)	266.2	265
	2.3	30	40						0 (sleeper/ballast)	302.9	295
	2.4	30	75						0 (sleeper/ballast)	317.5	325
3	3.1	25	40	210	3.055	2.50	0.26	0.60	0 (sleeper/ballast)	286.8	285
									0.30 (ballast/sub-ballast)	89.7	100
	3.2	25	80						0 (sleeper/ballast)	302.4	315
	3.3	30	40						0 (sleeper/ballast)	344.1	335
	3.4	30	60						0 (sleeper/ballast)	353.9	355
4	4.1	22.5	60	210	3.055	2.60	0.30	0.60	0.90 (interlayer)	15.1	13
									2.30 (subgrade)	5.0	5.5
	4.2	10.5	60						0.90 (interlayer)	7.1	6
									2.30 (subgrade)	2.3	2
	4.3	22.5	200						0.90 (interlayer)	17.5	14
									2.30 (subgrade)	5.8	5.6
	4.4	10.5	200						0.90 (interlayer)	8.2	8
									2.30 (subgrade)	2.7	2.5
5	5.1	26	47.5	210	2.703	2.20	0.27	0.65	0.30 (ballast/earthfill)	114.4	100
									0.50 (earthfill)	95.5	95
									0.70 (earthfill)	81.4	85
									0.90 (earthfill)	70.5	77
									1.10 (earthfill/subgrade)	62.0	60
6	6.1	23	120	210	3.217	2.60	0.29	0.60	0.45 (sub-ballast/subgrade)	31.4	30
7	7.1	14	200	210	3.217	2.60	0.29	0.60	0.65 (sub-ballast/subgrade)	13.8	15
									0.90 (subgrade)	11.0	9
									1.15 (subgrade)	9.0	7
									1.45 (subgrade)	7.2	6
8	8.1	22.5	160	210	3.217	2.60	0.27	0.60	0.45 (ballast/subgrade)	37.9	35
9	9.1	19.6	65	210	2.703	2.50	0.26	0.60	0.40 (ballast/subgrade)	71.8	66
10	10.1	20.1	65	210	2.703	2.50	0.26	0.60	0.40 (ballast/subgrade)	75.5	68
	10.2	20	70						0.40 (ballast/subgrade)	81.7	87
11	11.1	20	70	210	2.703	2.40	0.27	0.60	0.40 (ballast/subgrade)	72.4	68

12	12.1	22.5	160	210	3.217	2.40	0.27	0.60	0.35 (ballast/subgrade)	46.2	44
13	13.1	22.5	5	210	3.217	2.40	0.28	0.60	0.45 (ballast/subgrade)	52.7	46.7
	13.2		80							59.3	48.1
	13.3		90							60.0	49.0
	13.4		100							60.7	58.4
	13.5		110							61.4	59.2
	13.6		120							62.0	58.3
14	14.1	14.5	5	210	3.217	2.50	0.28	0.60	0.40 (ballast/fill)	26.9	26.4
									0.80 (fill/subgrade)	9.2	9.8
	14.2		160						0.40 (ballast/fill)	33.0	32.9
									0.80 (fill/subgrade)	11.3	10.4
	14.3		180						0.40 (ballast/fill)	33.6	33.5
									0.80 (fill/subgrade)	11.7	10.6
	14.4		200						0.40 (ballast/fill)	34.2	33.7
									0.80 (fill/subgrade)	11.7	11.2
	14.5		250						0.40 (ballast/fill)	35.6	37.3
									0.80 (fill/subgrade)	12.1	10.7
15	15.1	25	75	210	3.055	2.20	0.26	0.60	0.45 (ballast/fill)	32.5	32
									0.65 (fill)	27.2	28
									0.95 (fill)	21.4	23
									1.15 (fill)	15.2	14
									1.45 (fill/subgrade)	9.8	10
									2.45 (subgrade)	7.3	8
									3.45 (subgrade)	5.7	5
16	16.1	34	300	210	3.217	2.60	0.29	0.60	0.30 (ballast)	170.6	170
17	17.1	13	0	210	3.055	2.50	0.29	0.65	0.40 (ballast/frost prot.)	20.3	20.0
									0.60 (frost protection)	9.8	8.5
	17.2		360						0.40 (ballast/frost prot.)	37.6	36.9
									0.60 (frost protection)	18.1	20.7
	17.3	17	0						0.40 (ballast/frost prot.)	26.6	27
									0.60 (frost protection)	12.8	13
	17.4		360						0.40 (ballast/frost prot.)	53.2	46
									0.60 (frost protection)	25.7	24
18	18.1	25.3	47.5	210	2.703	2.20	0.27	0.65	0.80 (structural fill)	$\sigma_z = 84.5$ $\sigma_x = 35.0$	$\sigma_z = 80.0$ $\sigma_x = 33.7$
19	19.1	13.5	108	210	3.038	2.50	0.30	0.65	0.90 (sub-ballast/subgrade)	22.8	21.6
									1.90 subgrade	12.0	10.8
									2.90 subgrade	7.1	7.9
20	20.1	25	80	210	3.217	2.50	0.30	0.54	0.50 (ballast/sub-ballast)	85.8	84.8
									1.10 (sub-ballast)	54.8	51.9
									3.00 (sub-ballast/embank.)	24.3	20.1
	20.2	30	70						0.50 (ballast/ sub-ballast)	101.3	100.5
									1.10 (sub-ballast)	64.8	63.6
									3.00 (sub-ballast/embank.)	28.8	27.4
	20.3	32.5	70						0.50 (ballast/ sub-ballast)	109.7	108.7
									1.10 (sub-ballast)	70.2	71.6
									3.00 (sub-ballast/embank.)	31.2	31.0
	20.4	35	70						0.50 (ballast/ sub-ballast)	118.2	116.6
									1.10 (sub-ballast)	75.5	78.5
									3.00 (sub-ballast/embank.)	33.6	34.8
21	21.1	21	60	210	3.055	2.50	0.26	0.60	0.15 (ballast)	$\sigma_z = 105.3$ $\sigma_x = 38.5$ $\sigma_y = 31.7$	$\sigma_z = 89.7$ $\sigma_x = 42.5$ $\sigma_y = 32.9$
									0.41 (capping)	45.5	45.0
									0.60 (subgrade)	34.9	38.1
	21.2	21	300						0.15 (ballast)	$\sigma_z = 131.5$ $\sigma_x = 48.1$ $\sigma_y = 39.6$	$\sigma_z = 108.5$ $\sigma_x = 53.4$ $\sigma_y = 45.4$
									0.41 (capping)	56.9	59.0
									0.60 (subgrade)	43.6	50.0

Note: stress values refer to the vertical direction σ_z unless otherwise indicated.

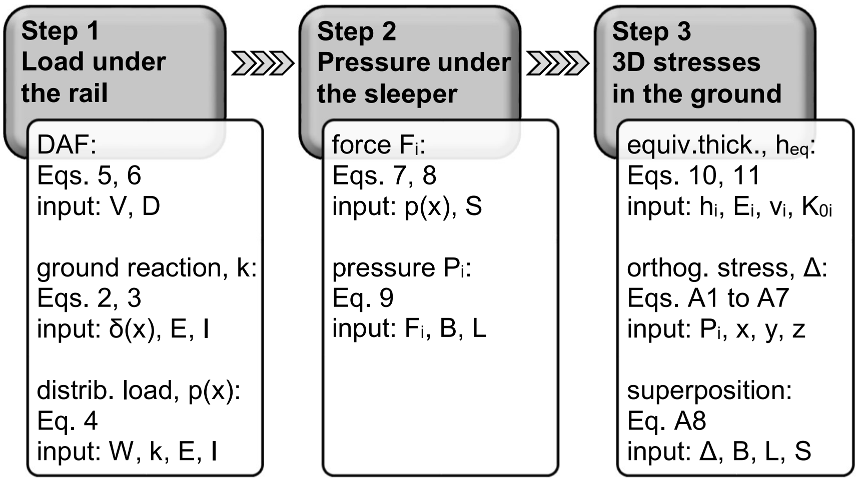

Figure 1. Flowchart with the calculation sequence.

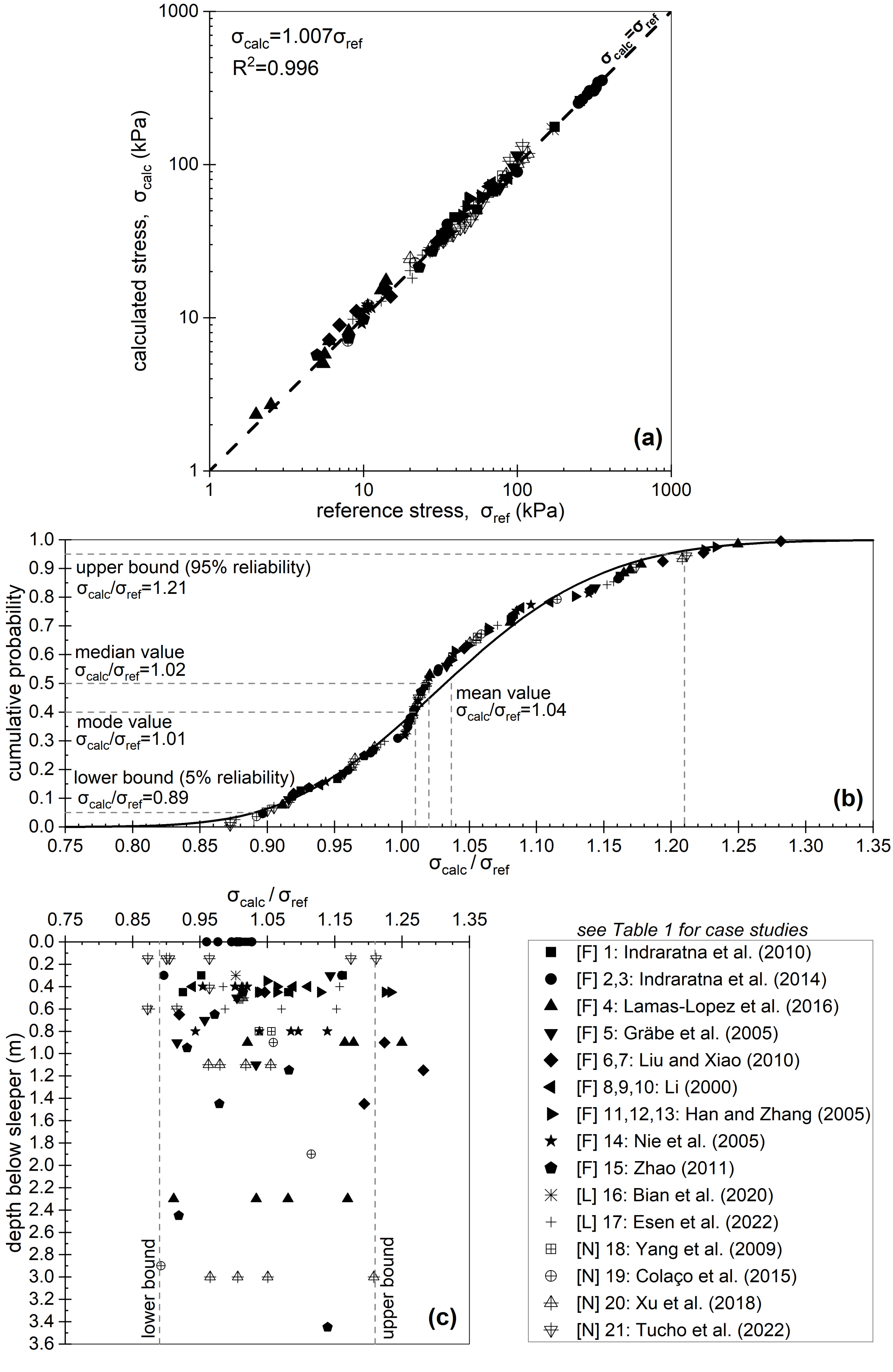

Figure 2. Validation of the analytical solution: (a) σ_{calc} versus σ_{ref}, (b) cumulative probability of occurrence of $\sigma_{calc}/\sigma_{ref}$, and (c) variation of $\sigma_{calc}/\sigma_{ref}$ with depth.

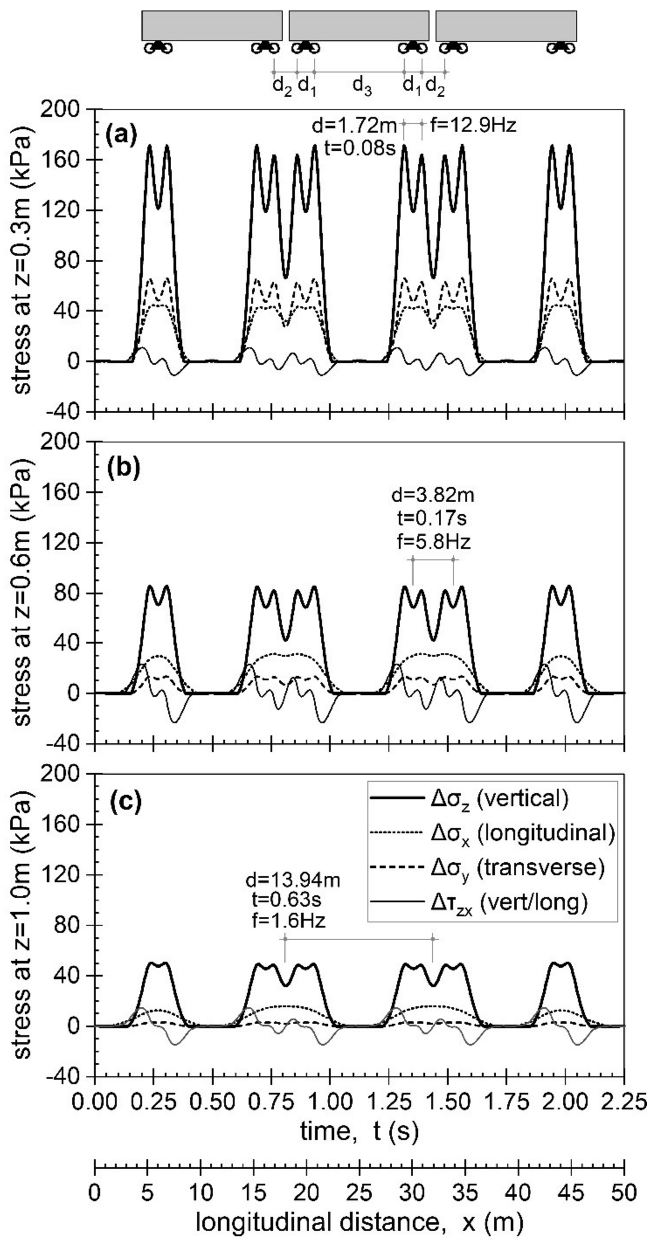

Figure 3. Stresses calculated for three wagons of Case A train, at the depths (a) 0.30 m, (b) 0.60 m, and (c) 1.0 m.

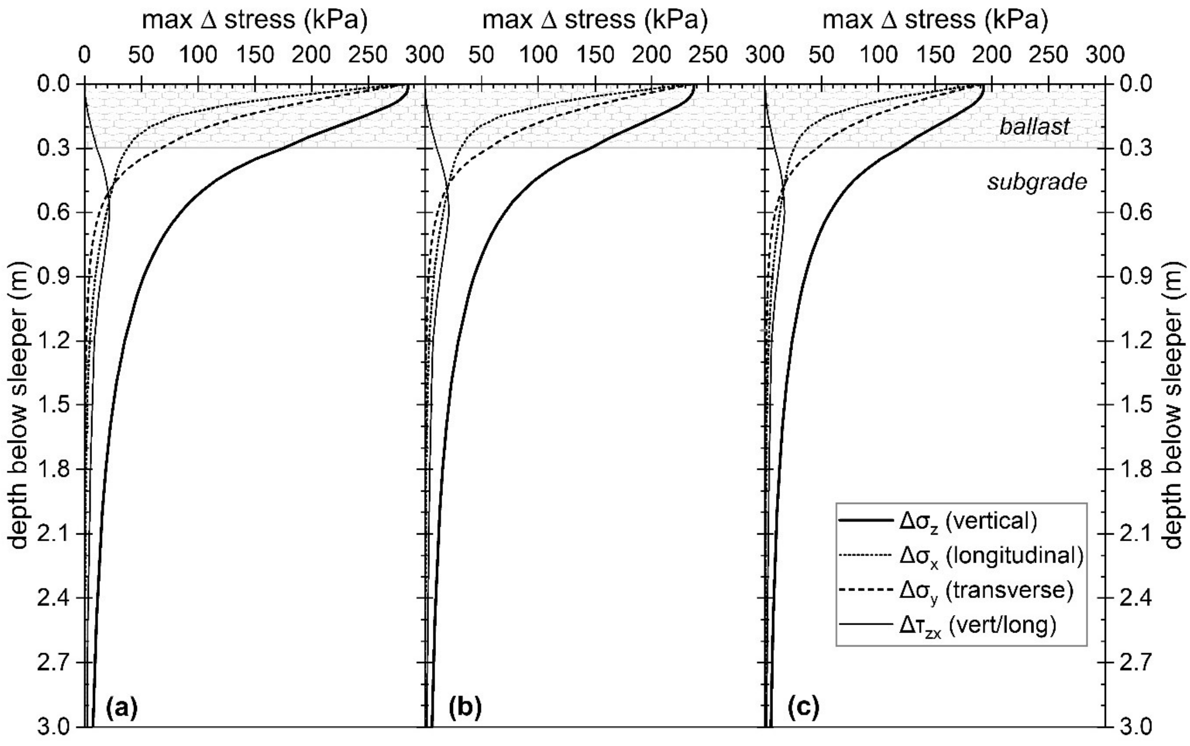

Figure 4. Variation of maximum stresses with depth for (a) Case A, (b) Case B, and (c) Case C.

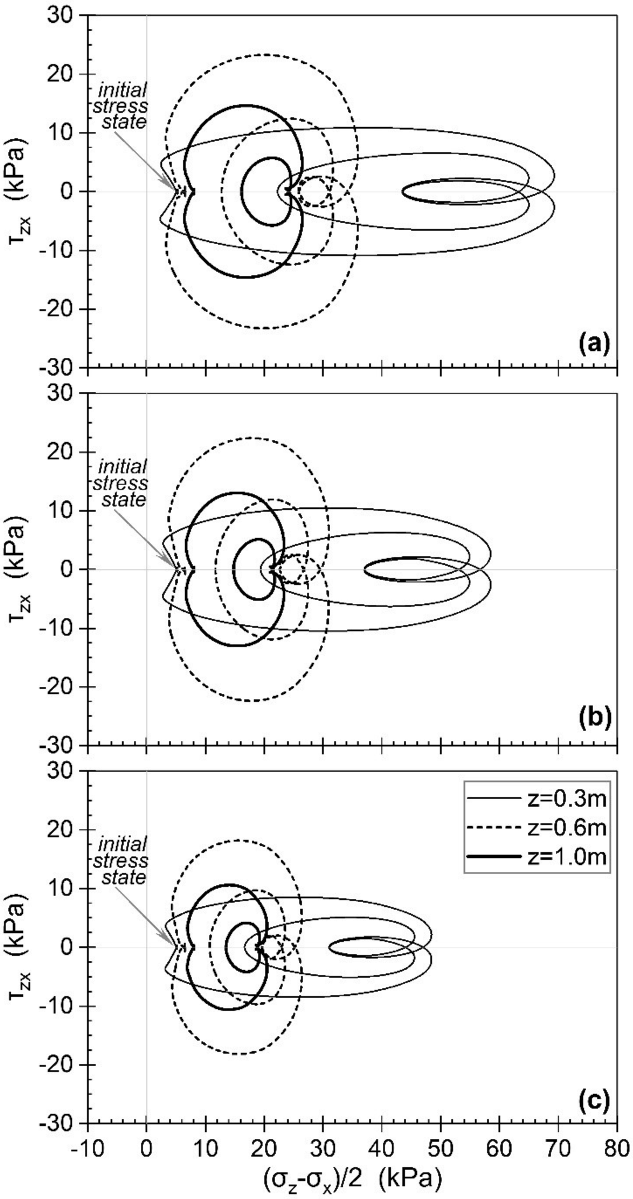

Figure 5. Cyclic stress paths for (a) Case A, (b) Case B, and (c) Case C.

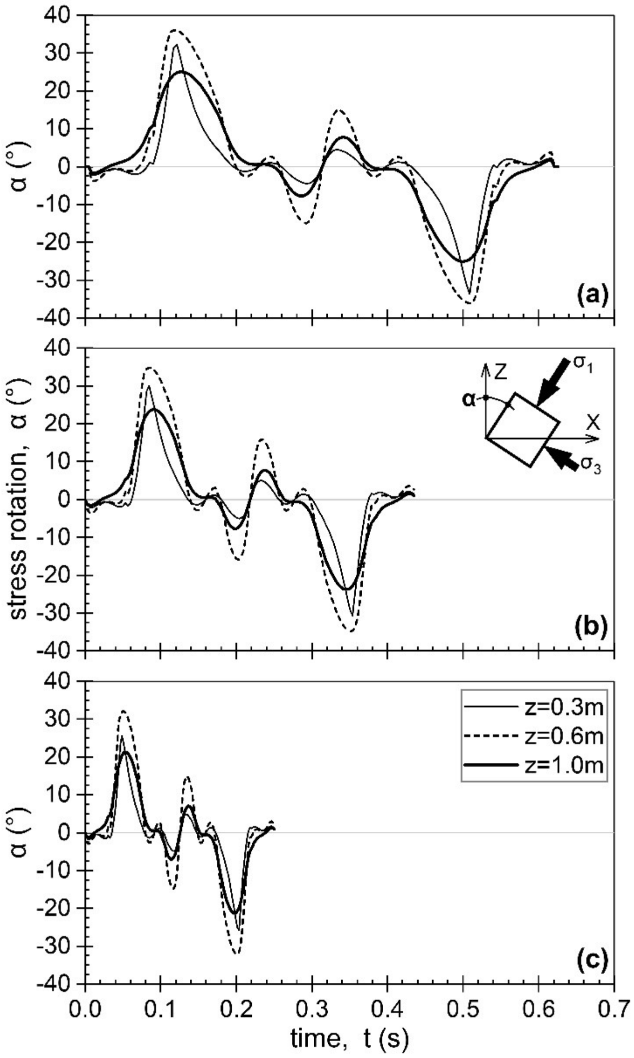

Figure 6. Major and minor principal stresses rotation angles for (a) Case A, (b) Case B, and (c) Case C.

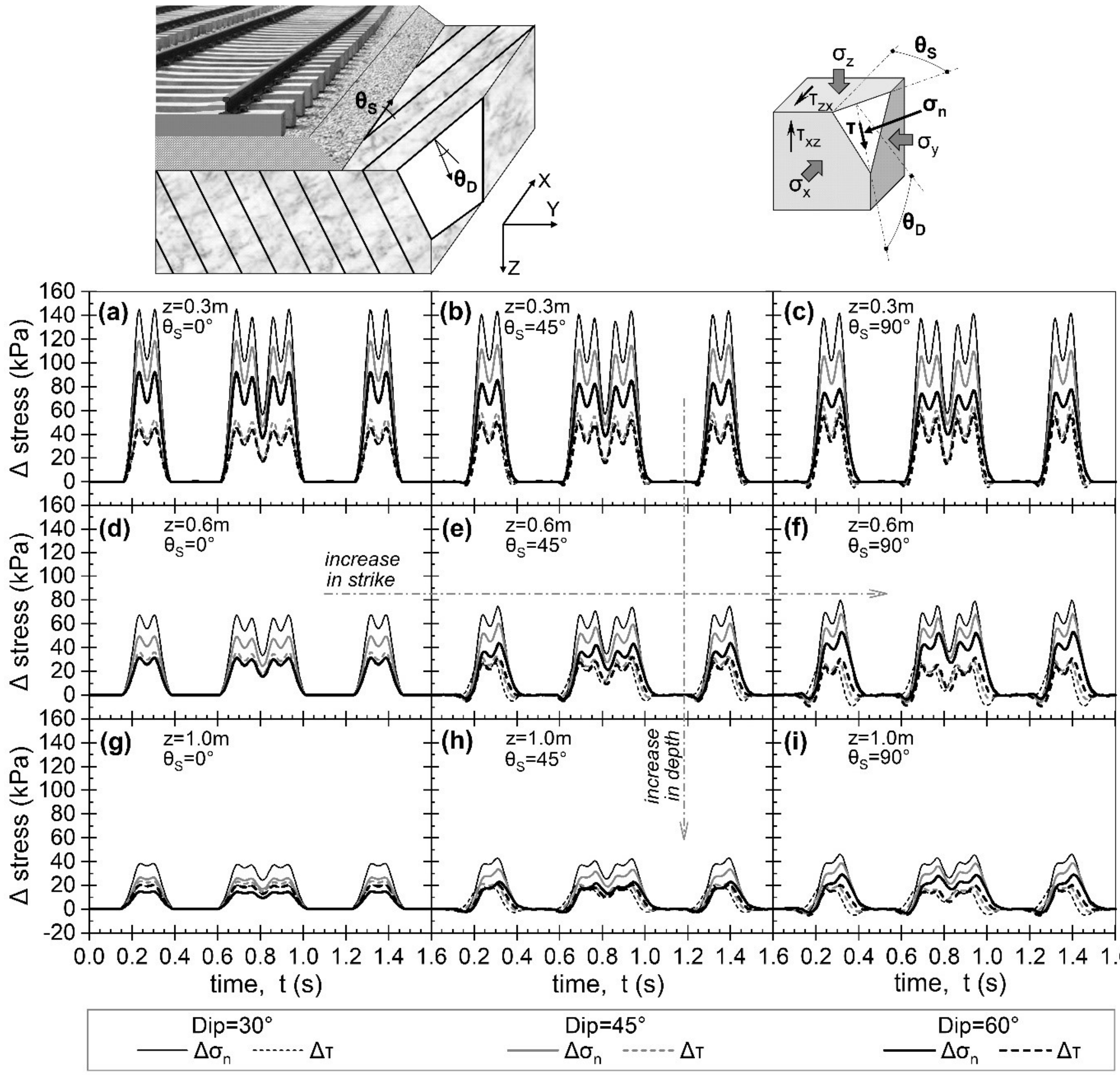

Figure 7. Normal and shear stresses on the discontinuity for Case A train at (a) (b) (c) z=0.3m, (d) (e) (f) z=0.6m, and (g) (h) (i) z=1.0m, with variable dip angles and (a) (d) (g) strike=0°, (b) (e) (h) strike=45°, and (c) (f) (i) strike=90°.

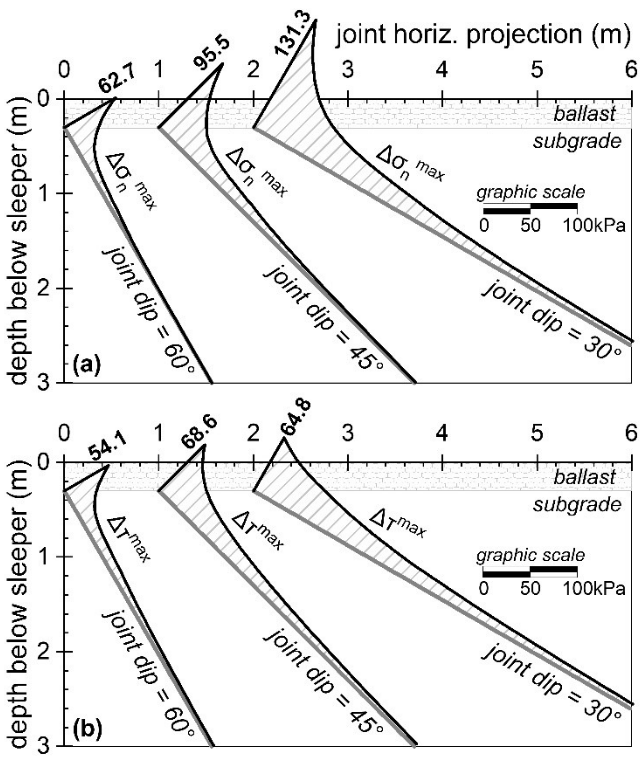

Figure 8. Variation of (a) maximum normal stress and (b) maximum shear stress along the joint length for Case A train, with strike=90° (transverse) and dip angles=30°, 45° and 60°.

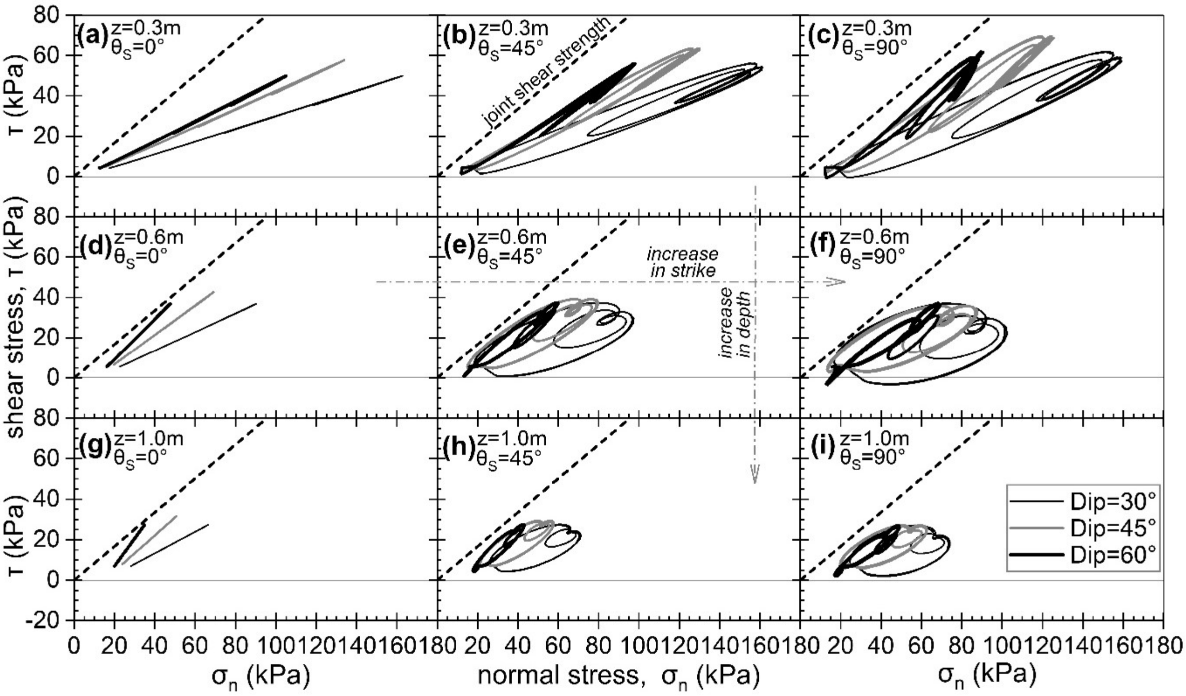

Figure 9. Cyclic stress paths on the discontinuity for Case A train at (a) (b) (c) z=0.3m, (d) (e) (f) z=0.6m, and (g) (h) (i) z=1.0m, with variable dip angles and (a) (d) (g) strike=0°, (b) (e) (h) strike=45°, and (c) (f) (i) strike=90°.

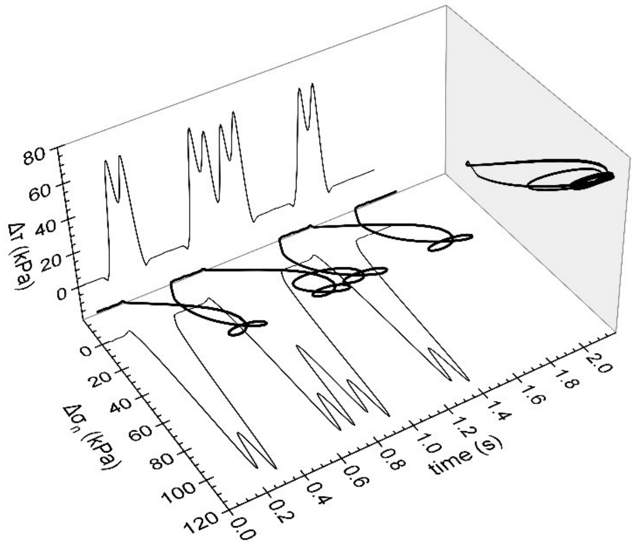

Figure 10. Cyclic stress path on the discontinuity for Case A train at the top of the subgrade (z=0.3m), for strike=90° (transverse) and dip=45°.

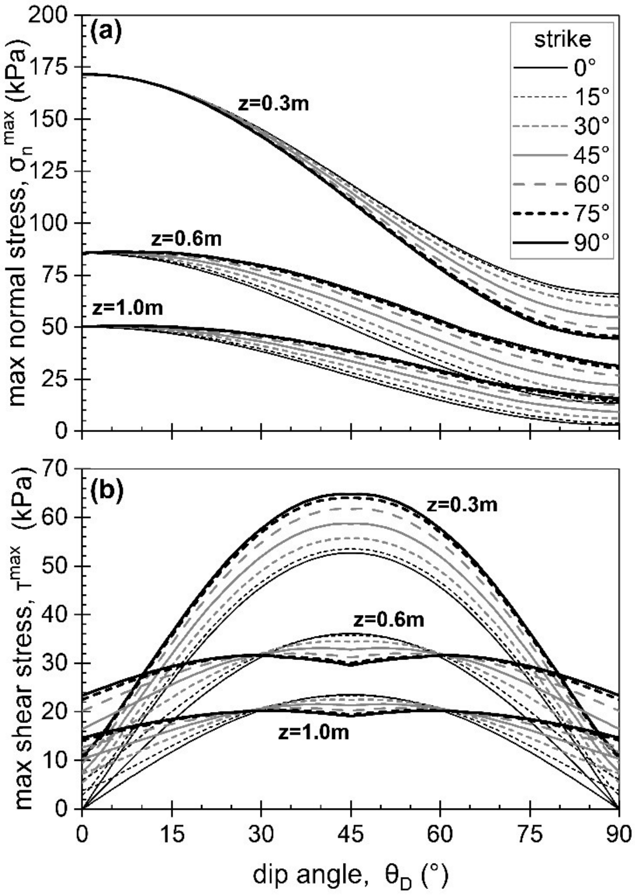

Figure 11. Influence of the discontinuity spatial orientation on the (a) normal stress and (b) shear stress, for Case A train and different depths.

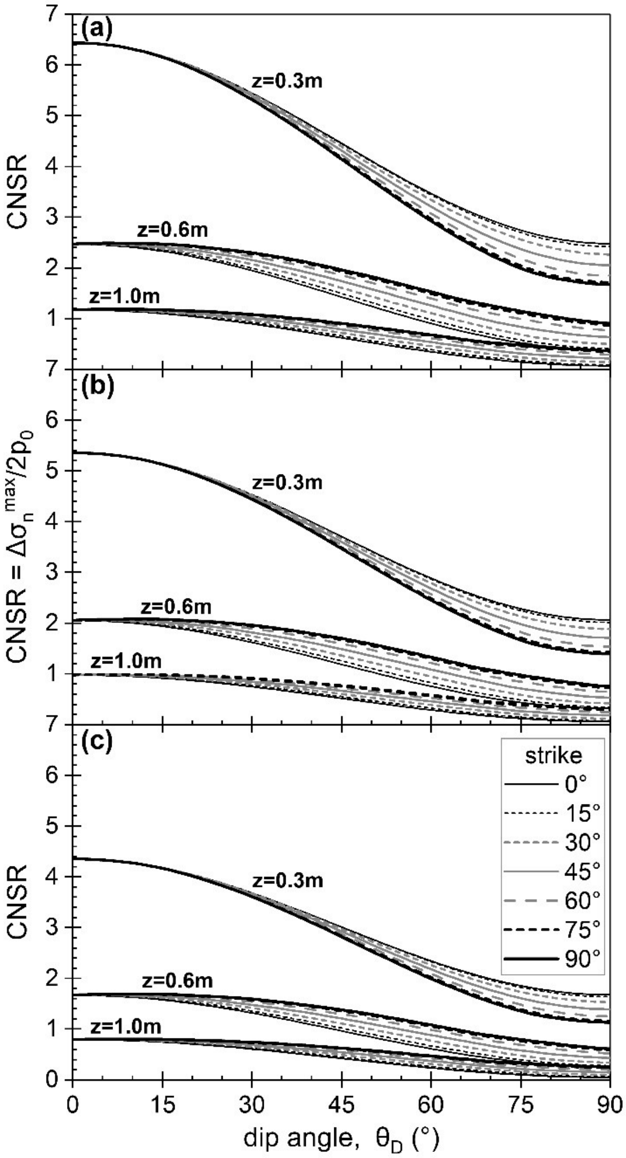

Figure 12. Influence of the discontinuity spatial orientation on the cyclic normal stress ratio for three different depths and (a) Case A, (b) Case B and (c) Case C.

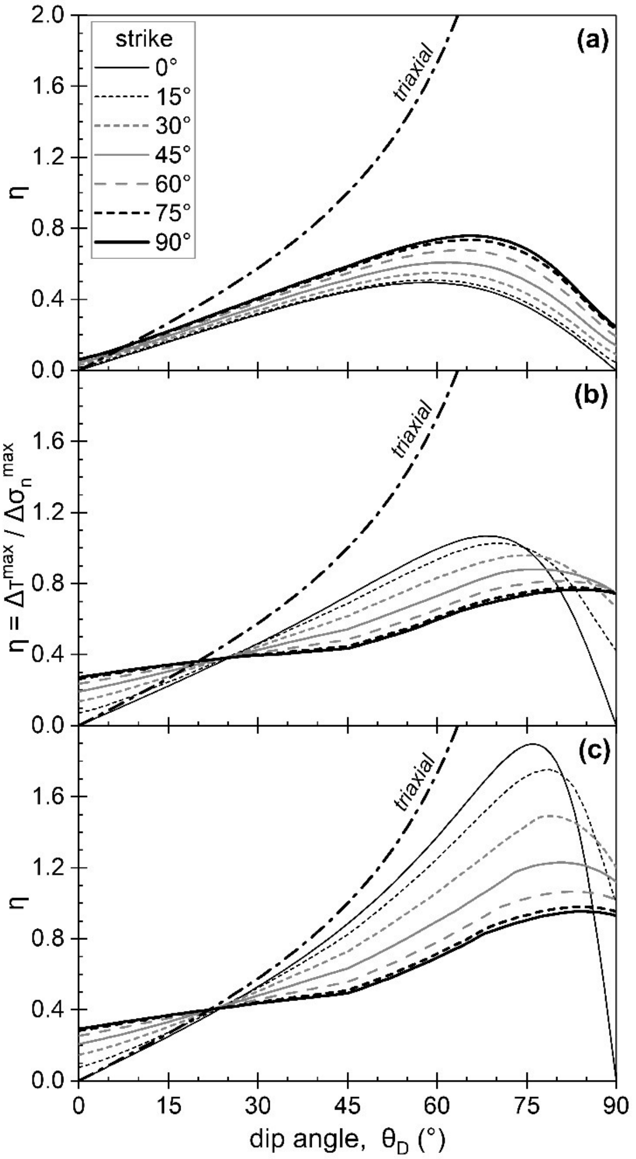

Figure 13. Influence of the discontinuity spatial orientation on the shear-to-normal stress ratio for the depths (a) z=0.3m, (b) z=0.6m and (c) z=1.0m, for Cases A, B and C (identical η for the three cases).

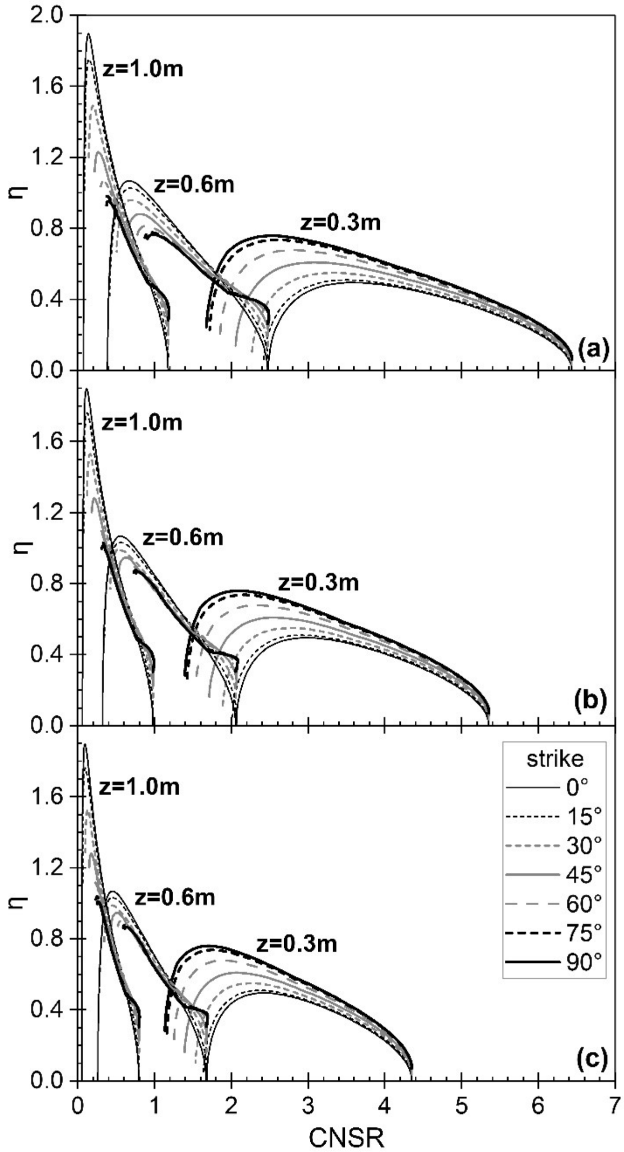

Figure 14. Relation between CNSR and η for different depths, discontinuity strikes and (a) Case A, (b) Case B and (c) Case C.

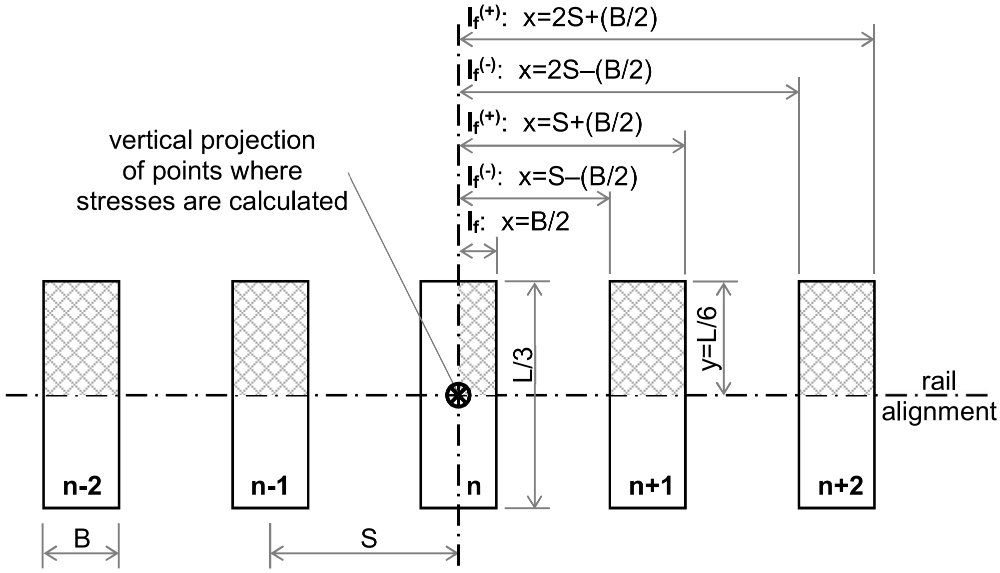

Figure A1. Plan view illustration of the superposition process to account for the influence of adjacent sleepers.